TEKTONIKA

Effect of Grain-Size and Textural Weakening in Polyphase Crustal and Mantle Lithospheric Shear Zones

Jonas B. Ruh *[1,2], **Whitney M. Behr** [1], **Leif Tokle** [1]

[1]Structural Geology and Tectonics Group, Geological Institute, Department of Earth Sciences, ETH Zürich, Zürich, Switzerland | [2]Institute of Marine Sciences, CSIC, Barcelona, Spain

Abstract Strain localization to form narrow plate boundary shear zones in Earth's lithosphere requires a significant amount of strain weakening. Here we investigate the relative contributions of grain-size-sensitive weakening versus textural weakening in polyphase shear zones in granitoid and peridotitic rocks through two-dimensional centimetre-scale bulk simple shear numerical models. The models deploy both constant grain size (only textural weakening) and dynamic grain-size evolution based on the paleowattmeter. Our results reveal that for granitoid rocks, textural weakening dominates, especially at temperatures around 550 °C, while grain-size-sensitive weakening plays a secondary yet significant role. For peridotitic rocks, intense weakening is evident below temperatures of ~1000 °C due to grain-size reduction, while textural weakening has a minor effect on weakening for experiments above 1000 °C. Two-dimensional experiments are compared to one-dimensional, single-phase models to reveal the effect of geometrical complexities in stress and grain-size evolution. These results are discussed in the context of natural lithospheric shear zones and are compared with established piezometers for individual mineral phases. Our findings underscore the vital role of grain-size-sensitive rheologies, particularly in the mantle lithosphere, for the initial weakening of ductile shear zones. These insights offer quantitative constraints that advance our understanding of the long-term strength of lithospheric plate boundaries.

Executive Editor:
Robin Lacassin
Associate Editor:
Dripta Dutta
Technical Editor:
Mohamed Gouiza

Reviewers:
Melanie Finch
Anonymous reviewer

Submitted:
31 August 2023
Accepted:
5 February 2024
Published:
14 March 2024

1 Introduction

Deformation at plate boundaries is characterized by the accumulation of strain along localized shear zones through the lithosphere. Localization and progressive accommodation of strain in shear zones requires a decrease of their strength in contrast to the surrounding weakly deformed host rock (*Bercovici*, 2003; *Braun et al.*, 1999; *Platt and Behr*, 2011; *Vauchez et al.*, 2012). Several processes have been proposed to contribute to ductile weakening during strain accumulation and thus localization of shear zones, such as shear heating (*Duretz et al.*, 2015; *Hartz and Podladchikov*, 2008), development of a mechanical anisotropy defined by a crystal-preferred orientation (*Bystricky et al.*, 2000), metamorphic reactions leading to growth of weaker phases (*Ceccato et al.*, 2018; *Goncalves et al.*, 2012; *Oliot et al.*, 2010), partial melting (*Tommasi et al.*, 1994), geometric reorganization of minerals resulting in textural anisotropy (*Dabrowski et al.*, 2012; *Ji et al.*, 2004; *Montési*, 2013; *Rast and Ruh*, 2021), and strain-dependent reduction of grain size and the consequent activation of grain-size-sensitive creep as the dominant deformation mechanism (*Platt and Behr*, 2011; *Ruh et al.*, 2022; *Warren and Hirth*, 2006).

Of the many possible mechanisms that can induce strain localization, the coalescence of weak phases to form strong layering and, simultaneously, intense grain-size reduction, are both ubiquitous features of natural high strain shear zones (i.e., mylonites), and are thus expected to be two of the most efficient mechanisms of localizing strain (e.g., *Dabrowski et al.*, 2012; *Montési*, 2013; *Tokle et al.*, 2023). Several previous studies have examined the role of textural weakening in evolving ductile shear zones, where textural weakening refers to structural rearrangement and changes in size, shape, and crystallographic orientation of mineral crystals in a rock. *Montési* (2007), for example, presented a constitutive analytical model that suggests that textural weakening has a high localization potential compared to other weakening mechanisms. *Dabrowski et al.* (2012) applied a two-dimensional mechanical numerical model to demonstrate that initially isotropic rocks with weak inclusions initially harden up to a shear strain of γ = 1, followed by significant weakening and eventually the formation of typical S-C structures defined by connected

*✉ jruh@icm.csic.es

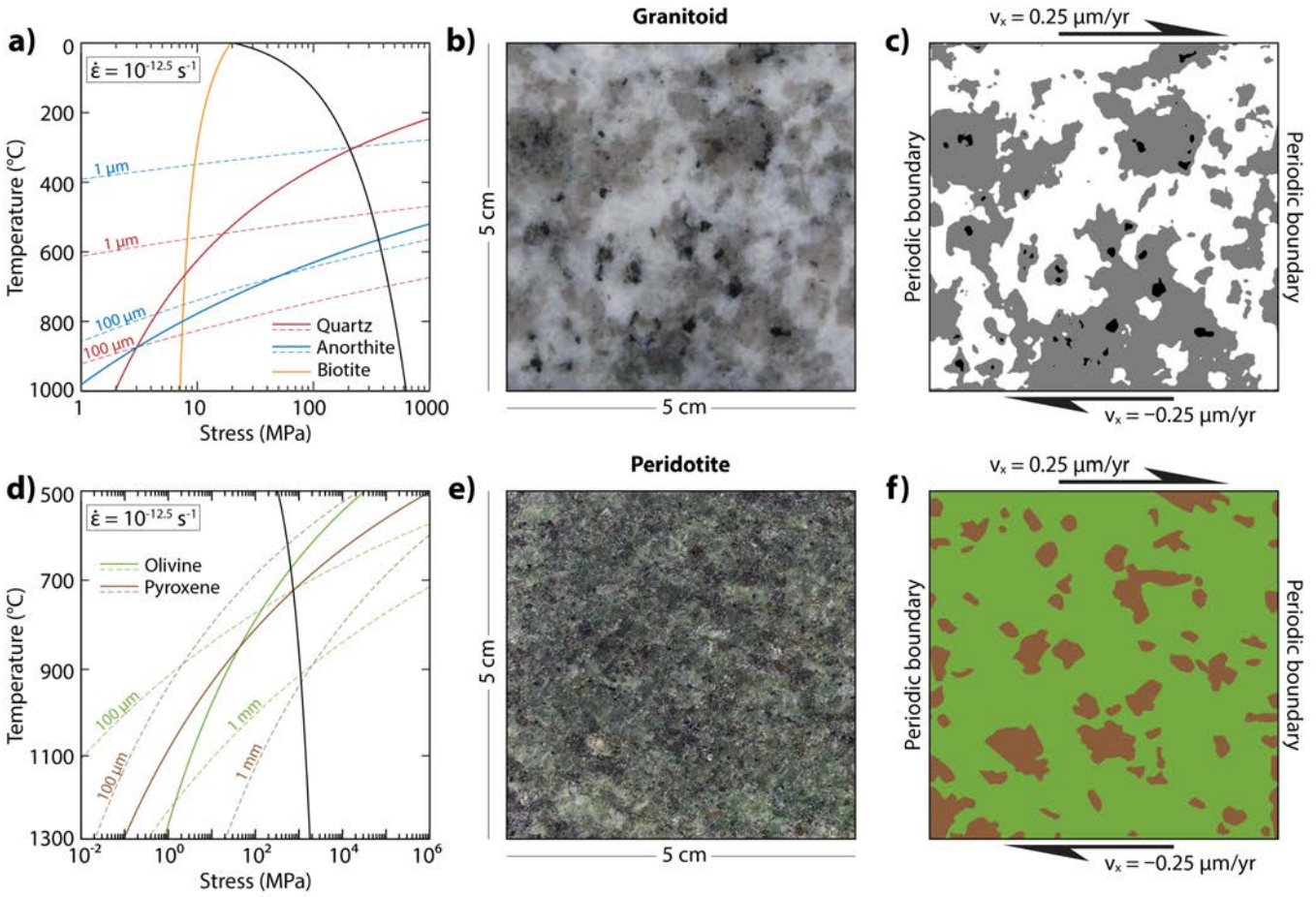

Figure 1 – Model setup and applied rheologies. **a)** Strength profiles for quartz (red) and anorthite (blue) for a strain rate of $10^{-12.5}$ s^{-1} (see Table 1 for references). Solid line: Dislocation creep. Dashed lines: Diffusion creep (at given grain size). Yellow line: Dislocation creep for biotite. Black line: Brittle yield envelope. **b)** Photographic image of a polished granite sample from the Rotondo granite, Central Swiss Alps. **c)** Digitalized image showing plagioclase (white), quartz (grey), and biotite (black). **d)** Strength profiles for olivine (green) and orthopyroxene (brown) for a strain rate of $10^{-12.5}$ s^{-1} (see Table 1 for references). Solid line: Dislocation creep. Dashed lines: Diffusion creep (at given grain size). Black line: Brittle yield envelope. **e)** Photographic image of a polished spinel-lherzolite sample from the Balmuccia body in the Ivrea Zone, European Southern Alps. **f)** Digitalized image showing olivine (green), and orthopyroxene (brown).

stretched weak inclusions. Furthermore, *Rast and Ruh* (2021) presented two-dimensional numerical shear experiments of quartz-biotite mixtures with a bulk-isotropic initial texture. Depending on the temperature range and the applied viscous flow laws, biotite appears either as weak or strong inclusions. Their results indicate that bulk rock strain weakening of a few percent coincides with the development of shear-parallel biotite bands, which only occurs when biotite is weaker than quartz (T < 450 °C), consistent with recent deformation experiments on aggregates of quartz and muscovite *Tokle et al.* (2023). Altogether, texture-related weakening has been shown to exhibit a significant localization potential if the strength of initially unconnected inclusions is sufficiently weaker than the matrix.

The role of grain-size reduction on strain localization has also been investigated in previous studies (e.g., *Hirth and Kohlstedt*, 2003; *Rybacki and Dresen*, 2000), typically through deformation mechanism maps and/or one-dimensional grain-size-evolution models that incorporate grain-size-sensitive flow laws and grain growth formulations (e.g., *Austin and Evans*, 2007; *Braun et al.*, 1999; *De Bresser et al.*, 2001; *Hopper and Buck*, 1993; *Rutter and Brodie*, 2004). Strength profiles of crustal (quartz-anorthite) and mantle (olivine-orthopyroxene) mineral assemblages illustrate the general trends that smaller grain sizes result in a weaker grain-size-sensitive rheology (Figure 1a,d). *Braun et al.* (1999) used a simple grain-size evolution parameterization to demonstrate the high potential for localization during cooling and exhumation of lithospheric shear zones, as commonly observed in nature (*Platt and Behr*, 2011). *Montési* (2013) analytically demonstrated that the localization potential of grain-size reduction can be significant also in high temperature shear zones. Such grain-size-evolution models typically consist of terms for grain growth based on experimental data (*Dresen et al.*, 1996; *Speciale et al.*, 2020; *Tokle and Hirth*, 2021), and grain-size reduction calculated by energy balance (*Austin and Evans*, 2007; *Bercovici et al.*, 2001; *Rozel et al.*, 2011). Recently, two- and three-dimensional thermo-mechanical numerical

Table 1 – Rheological, mechanical, and grain-size evolution parameters.

Dislocation creep					
	Quartzite	Anorthite	Biotite	Olivine	Orthopyroxene
A_D ($Pa^{-n}·s$)	$1.75·10^{-36}$	$1.585·10^{-18}$	$2.05·10^{-134}$	$9·10^{-20}$	$1.1·10^{-7}$
n (-)	4	3	18	3.5	3
m (-)	0	0	0	0	0
Q (kJ/mol)	125	$345+3.8·10^{-5}·P$	51	$480+1.1·10^{-5}·P$	603
r (-)	1	1	0	1.2	0
Reference	*Tokle et al.* (2019)	*Rybacki et al.* (2006)	*Shea and Kronenberg* (1992)	*Hirth and Kohlstedt* (2003)	*Zhang et al.* (2020)

Diffusion creep					
	Quartzite	Anorthite	Biotite	Olivine	Orthopyroxene
A_D ($Pa^{-n}·m^{-m}·s$)	$6.31·10^{-19}$	$1.995·10^{-25}$	-	10^{-27}	$2.019·10^{-27}$
n (-)	1	1	-	1	1
m (-)	2	3	-	3	3
Q (kJ/mol)	220	$159+3.8·10^{-5}·P$	-	$335+0.4·10^{-5}·P$	$200+1.4·10^{-5}·P$
r (-)	1	1	-	1	0.7
Reference	*Brodie and Rutter* (2000)	*Rybacki et al.* (2006)	-	*Hirth and Kohlstedt* (2003)	*Zhang et al.* (2017)

Frictional strength					
	Quartzite	Anorthite	Biotite	Olivine	Orthopyroxene
φ (°)	35	35	5	35	35
C (MPa)	25	25	130	25	25
Reference	*Schön* (2015)	*Schön* (2015)	*Shea and Kronenberg* (1992)	*Schön* (2015)	*Schön* (2015)

Grain size reduction					
	Quartzite	Anorthite	Biotite	Olivine	Orthopyroxene
λ_{init} (-)	0.00015	0.0001	-	0.0001	0.0001
λ_{stat} (-)	0.015	0.01	-	0.01	0.01
c (-)	3.142	3.142	-	3.142	3.142
g (J/m^2)	1	1	-	1	1
Reference	*Tokle and Hirth* (2021)	*Austin and Evans* (2007)	-	*Ruh et al.* (2022)	*Austin and Evans* (2007)

Grain growth					
	Quartzite	Anorthite	Biotite	Olivine	Orthopyroxene
A_g ($m^{-p}·s^{-1}·Pa^{-rg}$)	$2.61·10^{-19}$	$2.59·10^{-4}$	-	$3·10^{-6}$	3.17*
Q_g (kJ/mol)	134	365	-	$620+0.5·10^{-5}·P$	720
p (-)	3	2.6	-	3.2	2.4
r_g (-)	1.38	0	-	1	1
Reference	*Tokle and Hirth* (2021)	*Dresen et al.* (1996)	-	*Speciale et al.* (2020)	*Skemer and Karato* (2007)

* Adapted for variable fugacity

experiments with composite dislocation-diffusion creep coupled to such grain-size-evolution models demonstrated that these parameters have major effects for a variety of tectonic processes, such as rifting (*Ruh et al.*, 2022), subduction (*Gerya et al.*, 2021), the formation of transform faults (*Schierjott et al.*, 2020a), and mantle convection (*Dannberg et al.*, 2017; *Fuchs and Becker*, 2019; *Schierjott et al.*, 2020b).

Despite substantial efforts to understand the large-scale implications of coupling a self-consistent grain-size evolution to grain-size-sensitive rheological models, there are two open questions this study plans to address, particularly related to their importance during the initiation, and thus weakening, of small-scale shear zones: i) To what extent do grain size and textural evolution interact with each other to promote strain weakening and shear zone formation? ii) Which mechanism is more important for the localization in nascent crustal and mantle shear zones?

Here we attempt to answer these questions by applying a centimeter-scale two-dimensional numerical model that combines brittle and ductile (dislocation and diffusion) creep rheologies in polyphase aggregates of generic granitoid crustal and peridotitic mantle compositions. During imposed bulk simple shear, numerical experiments track the evolving complex textures and grain-size evolution through application of reduction and growth terms following the paleowattmeter (*Austin and Evans*, 2007). Complex two-dimensional shear experiments are compared to the stress evolution of one-dimensional single-phase experiments. The advantage of our two-dimensional shear experiments over one-dimensional analytical models include i) the development of shear-related textures that affect rock strength, ii) realistic local stress distributions, iii) contribution of a brittle component of deformation to textural rearrangement, and iv) the ability to track bulk shear zone strength. We show that both textural weakening and grain-size reduction contribute substantially to strain localization in specific parts of the granitoid crust and the mantle

lithosphere.

2 Methods

Both one- and two-dimensional numerical codes rely on the same rheological and grain-size-evolution parameters and are provided in the Supporting Information (Supplementary Code). The applied two-dimensional numerical code is based on the finite difference method with a fully staggered Eulerian grid and Lagrangian markers. Governing equations include conservation of mass (incompressible):

$$\frac{\partial u_i}{\partial u_j} = 0 \tag{1}$$

and conservation of momentum

$$\frac{-\partial P}{\partial u_i} + \frac{\partial \tau_{ij}}{\partial x_j} = 0 \tag{2}$$

where P is dynamic stress, u_i are velocities, x_i are spatial coordinates and τ_{ij} the deviatoric stress tensor. The equations are discretized on the Eulerian domain and solve for velocity and pressure. Velocities on the nodes are interpolated onto Lagrangian markers following the fourth-order Runge-Kutta method.

2.1 Rheological Model

The code employs a visco-elasto-plastic rheology, where the visco-elastic stresses and strain rates depend on a Maxwell relationship

$$\dot{\varepsilon}_{ij} = \frac{1}{2\eta_v}\tau_{ij} + \frac{1}{2G}\frac{D\tau_{ij}}{Dt} \tag{3}$$

where G is the shear modulus (100 GPa for all phases) and η_v is viscosity. Dislocation and diffusion creep viscosities are calculated independently following the equation of viscous flow

$$\eta_{disl,diff} = 0.5 \cdot \frac{1}{A_D f_{H_2O}^r} \cdot \tau_{II}^{(1-n)} \cdot d^{-m} \cdot exp\left(\frac{Q}{RT}\right) \tag{4}$$

where τ_{II} is the second invariant of the stress tensor of the previous time step:

$$\tau_{II} = \sqrt{\frac{1}{2}\tau_{ij}^2} \tag{5}$$

A_D is the pre-exponent, f_{H_2O} is water fugacity, r is the water fugacity exponent, n is the stress exponent, d is grain size, m is the grain size exponent, Q is the activation enthalpy and R is the gas constant. The composite viscosity is as calculated by

$$\eta_v = \left(\frac{1}{\eta_{disl}} + \frac{1}{\eta_{diff}}\right)^{-1}. \tag{6}$$

Plastic failure occurs if the visco-elastic differential stresses exceed a yield stress based on the Drucker-Prager yield criterion

$$\sigma_y = P \cdot \sin\varphi + C \cdot \cos\varphi \tag{7}$$

resulting in a plastic viscosity of

$$\eta_p = \frac{\sigma_y}{2\dot{\varepsilon}_{II}} \tag{8}$$

where C is cohesion, φ is the friction angle and $\dot{\varepsilon}_{II}$ is the second invariant of the strain rate tensor,

$$\dot{\varepsilon}_{II} = \sqrt{\frac{1}{2}\dot{\varepsilon}_{ij}^2}\,. \tag{9}$$

The viscosity going into the Maxwell rheological model follows $\eta = min(\eta_v, \eta_p)$. Elasticity is implemented by adapting the viscosity η_v by a visco-elasticity factor Z and updating stresses as a function of the stress history with an elastic time step of 100 yr (*Moresi et al.*, 2003; *Ruh and Vergés*, 2018)

$$Z = \frac{\Delta t \cdot G}{\eta_v + \Delta t \cdot G} \tag{10}$$

$$\eta_{ve} = \eta_v \cdot Z = \frac{\eta_v \cdot \Delta t \cdot G}{\eta_v + \Delta t \cdot G} \tag{11}$$

$$\frac{D\tau_{ij}}{Dt} = \frac{\tau_{ij} - \tau_{ij}^{old}}{\Delta t} \tag{12}$$

where

$$\tau_{ij} = 2\eta_v\dot{\varepsilon}_{ij}Z + \tau_{ij}^{old}(1 - Z)\,. \tag{13}$$

Visco-elasto-plastic viscosities are forced to remain between lower and upper cutoffs of 10^{14} and 10^{24} Pa·s, respectively.

2.2 Grain-size Evolution

Grain-size evolution in our models is implemented by an independent assessment of reduction and growth terms based on the paleowattmeter (*Austin and Evans*, 2007). The observation that grain growth rates during diffusion creep are equal to static growth rates (*Walker et al.*, 1990) led to the conclusion that mechanical work related to diffusion creep is fully dissipated (*Austin and Evans*, 2007). Therefore, grain-size reduction rate is solely dependent on work produced by dislocation creep ($\sigma\dot{\varepsilon}_{disl}$). For simplicity, grain-size reduction is switched off if the mineral phase deforms brittle/plastically (here, a phase is considered to deform brittle if >3% of the mineral phase's markers exceed the plastic yield envelope, evaluated at every time step). Grain-size reduction related to brittle deformation is ignored due to lack of quantitative constrain. The following reduction term is described as

$$\dot{d}_{red} = \frac{\sigma\dot{\varepsilon}_{disl}\lambda d^2}{c\gamma_d} \tag{14}$$

where σ is stress, $\dot{\varepsilon}_{disl}$ is dislocation creep strain rate, c is a geometric constant (π for spherical grains), γ_d is the grain boundary energy, and λ denotes the fraction of work that goes into grain-size reduction. In both naturally and experimentally deformed samples, dynamic recrystallization is a

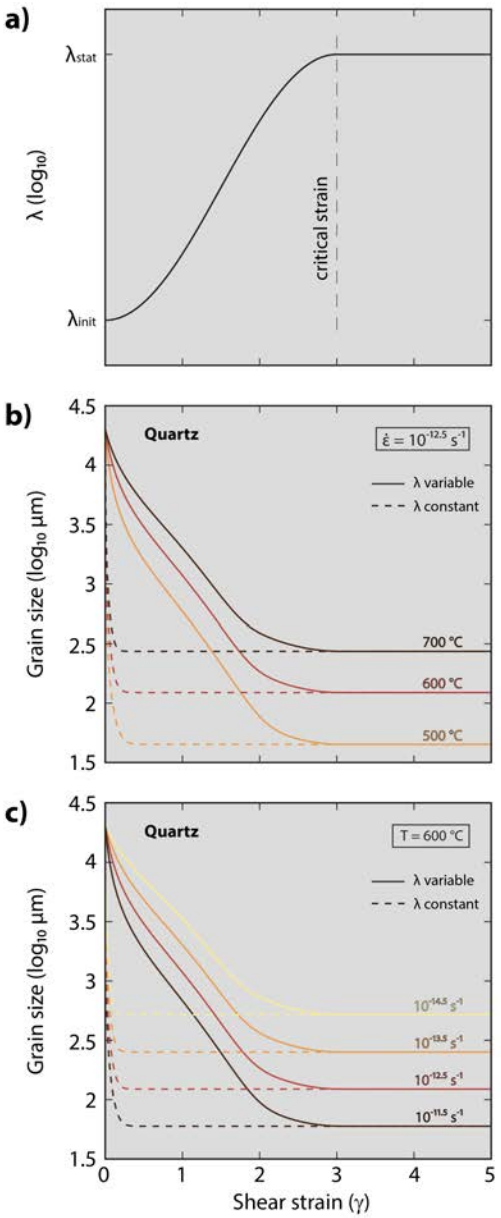

Figure 2 – Strain-dependent evolution of λ. **a)** λ increases from an initial value (λ_{init}) to a static value (λ_{stat}) between strain ε = 0–3. Values for λ_{init} and λ_{stat} for each mineral phase are given in Table 11. **b)** Grain-size evolution of quartz at different temperatures with initially increasing λ (full lines) versus constant λ_{stat} (dashed lines). **c)** Grain-size evolution of quartz at different strain rates with initially increasing λ (full lines) versus constant λ_{stat} (dashed lines).

progressive process where the amount of dynamic recrystallization increases with increasing strain (*Cross and Skemer*, 2019; *Heilbronner and Tullis*, 2006). To implement this effect into our models, we start with an initial (λ_{init}) value that then increases to its long-term static value (λ_{stat}) between a viscous shear strain of 0 and 3 (Figure 2a) similar to *Herwegh et al.* (2014). Long-term values (λ_{stat}) for quartz (0.015; *Tokle and Hirth*, 2021) and olivine (0.01; *Ruh et al.*, 2022) are taken from the literature, while values for anorthite and pyroxene were both assumed to be 0.01 as there are no current experimental values. Strain-dependence of λ follows a logarithmic sinusoidal relationship adapted and simplified from strain-dependent amount of recrystallization in olivine (*Cross and Skemer*, 2019). This is consistent with experimentally deformed quartzite in the general shear geometry, where samples achieve ~50-100% dynamic recrystallization by a shear strain of ~3 (*Heilbronner and Tullis*, 2006; *Richter et al.*, 2018; *Tokle et al.*, 2023). Without accounting for this strain-dependent increase of λ, our models show complete dynamic recrystallization within shear strains of <0.5, which is unrealistic in both natural and experimental samples (Figure 2b,c).

Grain growth rate is described by

$$\dot{d}_{gr} = A_g f_{H_2O}^{r_g} \exp\left(-\frac{Q_g}{RT}\right) p^{-1} d^{1-p} \qquad (15)$$

where A_g is the growth rate constant, f_{H_2O} is water fugacity, Q_g is activation potential,T is temperature, R is the gas constant, d is grain size and p is the growth exponent (Table 1). Each time step a new grain size d_{new} is calculated on the Lagrangian markers combining the reduction and growth components after solving the rheological equations,

$$d_{new} = (\dot{d}_{gr} - \dot{d}_{red}) \cdot Dt \qquad (16)$$

and is integrated into the viscosity calculation for diffusion creep (equation 4).

2.3 Initial Model Setup

Numerical experiments are designed to investigate meso-scale granitoid crustal and peridotitic mantle shear deformation. The Eulerian domain of all presented numerical experiments describes a square of 5 x 5 cm with a resolution of 401 x 401 nodes. Each nodal cell initially contains 16 Lagrangian markers, on which material properties and rock composition are stored. This implementation implies that each marker contains an individual value for grain size, independent of the mesoscopic textural context, but solely dependent on the local thermo-mechanical characteristics, in contrast to alternative studies investigating ductile shear zones (e.g., *Finch et al.*, 2020). The geometric setup and distribution of rock phases in numerical experiments is digitized from equally-sized photographs of granite and peridotite hand specimens from the Rotondo granite, Central Alps (Figure 1b), and from a spinel-lherzolite from the Balmuccia body in the Ivrea Zone, European Southern Alps (Figure 1e), respectively. These two samples serve as typical examples of undeformed granitoid and peridotite, respectively. The main phases of each hand specimen photograph are discriminated by ImageJ (Schneider et al., 2012) to define the initial marker distribution. In case of the granitoid sample, quartz (52.4% of markers), plagioclase (64.4%) and biotite (1.2%) are distinguished by colour (Figure 1c). Quartz and plagioclase (here assumed anorthite) undergo dislocation and diffusion creep based on experimentally derived flow laws, while biotite deforms by dislocation glide (*Kronenberg et al.*, 1990) best represented by a dislocation flow

law (Table 1). Grain-size evolution of quartz and plagioclase (100% An) depends on published grain growth laws (equation 15) with initial numerical grain sizes of 2 cm, resembling the sample appearance (see *Rast et al.*, 2022) and generalized grain sizes of felsic magmatic rocks. The fugacity applied for flow laws and grain growth refers to fluid saturation calculated after (*Shinevar et al.*, 2015). For the peridotite sample, olivine and pyroxene (here assumed 100% orthopyroxene) are distinguished by color, representing 81% and 19% of the total marker distribution, respectively (Figure 1f). Both components deform by experimentally derived composite diffusion-dislocation creep (Table 1). All applied olivine and pyroxene flow laws, and the olivine grain growth law, are obtained at hydrous conditions. However, only a dry (50 ppm H/Si) growth law exists for pyroxene (Table 1). To convert this dry condition to a hydrous one, the growth rate constant Ag for pyroxene is multiplied by twelve, resulting in a pseudo-hydrogen concentration of 600 ppm H/Si, better representing the conditions of the applied flow laws. Initial numerical grain sizes of olivine and pyroxene measure 5 mm, in accordance with undeformed natural peridotites (e.g., *Matysiak and Trepmann*, 2015). Fugacity for flow laws and grain growth of both olivine and pyroxene represents a moderate hydrogen concentration of 600 ppm H/Si and growth rate constants are adjusted accordingly (Table 1).

2.4 Boundary Conditions

Boundary conditions at the top and the bottom of the Eulerian domain describe a horizontal velocity of 0.25 and –0.25 µm/yr, respectively, which results in a background shear strain rate of $10^{-12.5}$ s^{-1} (Figure 1c,f). Lateral boundaries prescribe periodic conditions with vertical free slip, i.e. markers exiting the Eulerian domain on one side enter on the other, resulting in a constant number of Lagrangian markers during experiment evolution. Time stepping is set to 100 yr but may be shorter to conform to a Courant number of 0.2, defining the maximum relative distance a marker is allowed to travel between two nodes in one timestep. Experiments end when a background shear strain of γ = 20 is reached. To investigate the effect of grain-size-dependent weakening across a granitoid continental middle and lower crust, nine shear experiments were conducted at temperature conditions between 350–750 °C with 50 °C intervals, while confining pressures are calculated for a geotherm of 25 °C/km and a rock density of 2700 kg/m^3, corresponding to 371–795 MPa for the given temperature. To test the same effect through the mantle lithosphere, nine olivine-pyroxene experiments were performed with temperatures from 500 to 1200 °C with 100 °C intervals and confining pressures between 530 MPa–2.76 GPa, based on a mantle lithospheric geotherm of 10 °C/km and a rock density of 3250 kg/m^3. For both crustal and mantle rock assemblages, the same experiments were conducted where the initial grain size remains constant (2 cm for granitoid and 5 mm for peridotitic experiments) throughout the numerical experiment to distinguish the effects of grain-size-dependent weakening from purely textural weakening during shearing.

3 Results

A total of 46 numerical experiments were conducted for this study. The main article contains the results of 36 experiments representing variable pressure-temperature conditions and rock composition, and with dynamic grain-size evolution switched on or off. Additional experiments of granitoid mineral assemblage varying in initial grain size, initial geometric distribution, and without biotite are presented in Supporting Information to underline the robustness of the numerical approach (Supplementary Data). Hereafter, a selection of experiments is showcased that cover the critical observations. In addition to the results presented in the main article, animated graphics with the temporal evolution of all experiments are available in the Supporting Information (Supplementary Movies).

3.1 Granitoid Mineral Assemblage at Crustal Conditions

Figure 3 illustrates the textural evolution, viscosity distribution, grain sizes and deformation mechanism of granitoid numerical experiments with dynamic grain-size evolution after a bulk shear strain of γ = 20. For a temperature of 350 °C, the marker distribution shows unevenly distributed plagioclase clasts of variable sizes that developed by boudinage of the initially unfoliated texture and quartz-biotite bands connecting along the sense of shear (Figure 3a). Viscosity values for quartz exhibit ~10^{20} Pa·s, while viscosities for plagioclase represent either plastic shear bands due to stresses beyond the Drucker-Prager failure envelope or are capped by the upper cutoff (10^{24} Pa·s). After γ = 20, grain sizes are smaller for quartz (~10 µm) than for plagioclase (>1 mm). The dominant deformation mechanism of quartz is dislocation creep, while plagioclase deforms by brittle failure with background dislocation creep (Figure 3a). This background deformation mechanism in plagioclase indicates that for the applied flow laws at the given temperature-pressure conditions, dislocation creep results in a lower viscosity relative to diffusion creep, although both are beyond the upper cutoff (10^{24} Pa·s) and related strain rates are low.

At 500 °C, isolated sub-rounded plagioclase clasts develop in the lower part of the experiment after γ = 20, while the uppermost part remains largely undeformed (Figure 3b). The viscosity of quartz is lower than at 350 °C (10^{19}–10^{20} Pa·s) and viscosity of plagioclase remains high (>10^{23} Pa·s). Quartz

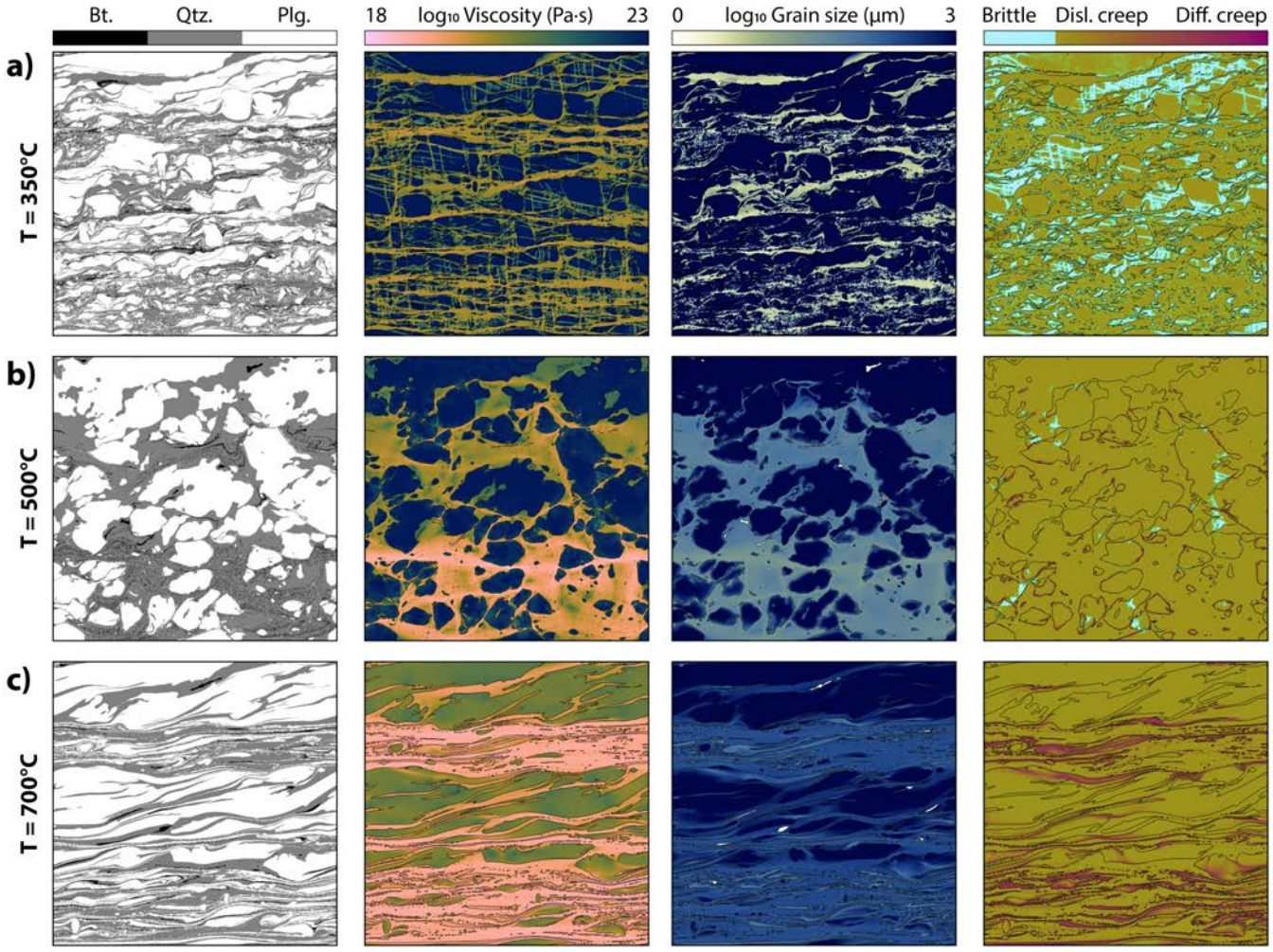

Figure 3 – Marker composition, viscosity, grain size, and deformation mechanism of numerical experiments with a granitoid crustal mineral assemblage after shear strain of γ = 20. a) 350 °C, b) 500 °C, c) 700 °C.

grain sizes are in the range of 100 μm, with values slightly lower where deformation localized (lower part of the model). Plagioclase grain sizes remain larger than 1 mm, except for the rims of rounded clasts, where it can decrease to values as low as ~100 μm (Figure 3b). At this temperature, quartz and plagioclase deform by dislocation creep, while plagioclase also shows localized regions of brittle deformation where plagioclase clasts collide. Diffusion creep is also active locally along the rims of plagioclase clasts, related to the occurrence of smaller grain sizes (Figure 3b).

At 700 °C, a clear foliation develops with distinct quartz and plagioclase mineral bands. Two zones of relatively less shearing occur in the centre and the uppermost ~1 cm of the model domain (Figure 3c). Complex plagioclase clasts with δ-tails, strain shadows, and asymmetric folding develop, consistent with the sense of shear. The viscosity of quartz is ~10^{19} Pa·s, while regions of elongated plagioclase show values up to 10^{21} Pa·s, depending on their size. Grain size of plagioclase in relatively low-strain regions remain large (>1 mm), while grain sizes of both quartz and plagioclase in the localized high-strain zones are roughly equal at ~100 μm (Figure 3c). Similar to the experiment at 500 °C, quartz deforms predominantly by dislocation creep, while plagioclase undergoes diffusion creep along the high-strained zones, and dislocation creep in the cores of large clasts defined by large grain sizes (Figure 3c).

The evolution of the average (natural logarithmic mean) quartz and plagioclase grain sizes during shearing depends on the temperature condition (Figure 4a,b). Initial quartz grain sizes of 2 cm reduce to quasi-constant values of ~5 μm at 350 °C after a bulk shear strain of ~5 and to 400 μm at 750 °C after a bulk shear strain of ~5 (Figure 4a). Plagioclase grain sizes at 350 and 400 °C remain constant at 2 cm because temperatures are too low for viscous creep to be activated and brittle-plastic deformation dominates instead (Figure 3a). Above 400 °C, plagioclase grain sizes reduce slower than quartz and show average values between ~2 mm at 450 °C to 300 μm at 750 °C after a shear strain of γ = 20 (Figure 4b). In contrast to quartz, plagioclase displays larger grain sizes at lower temperatures; however, grain-size evolution illustrates that steady-state conditions are not reached even by γ = 20 (Figure 4b).

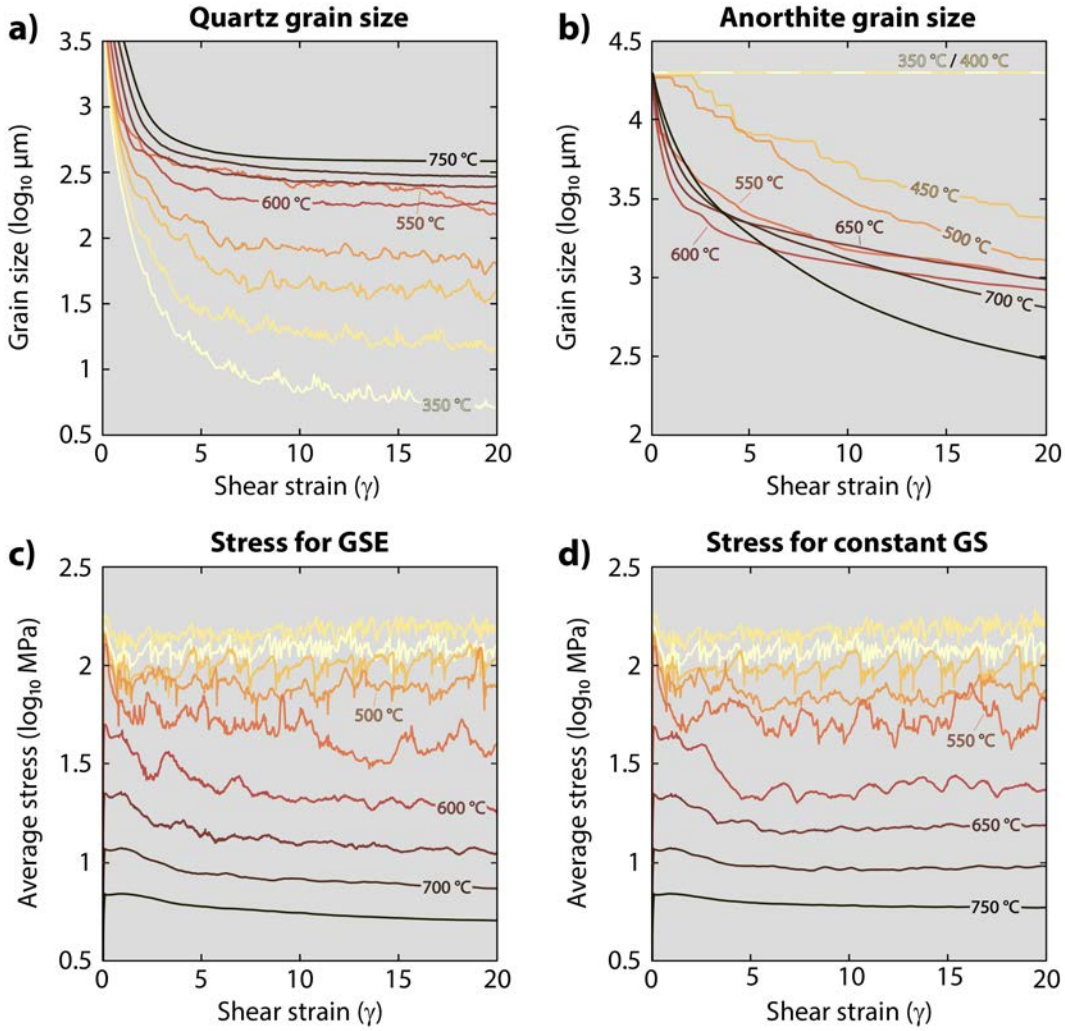

Figure 4 – Temporal evolution of grain-size and stress for crustal granitoid experiments. **(a)** Quartz and **(b)** anorthite grain size for experiments with dynamic grain size evolution. Average stress for **(c)** experiments with dynamic grain-size evolution (GSE) and for **(d)** experiments with constant grain size (constant GS).

The evolution of average stresses (harmonic mean of the second invariant of the stress tensor) for experiments both with (Figure 4c) and without (Figure 4d) dynamic grain-size evolution intuitively shows a strong temperature dependence. In both cases, stress evolution for low temperature experiments do not display significant stress loss, while experiments at intermediate temperatures (500–650 °C) experience the most weakening. For experiments with grain-size evolution, peak stresses developing after initial elastic loading range between ~7 MPa at 750 °C and 180 MPa at 350 °C (Figure 4c). After γ = 10, all experiments show generally stable average stress values between ~5 MPa and ~140 MPa for 750 °C and 350 °C, respectively, with important loss of strength at intermediate temperatures (Figure 4c). Stress evolution of experiments with constant grain sizes show similar stress peaks and slightly larger steady state stresses at intermediate temperatures of 500–600 °C (Figure 4d). Squiggly fluctuations in quartz grain size and stress evolution at temperatures up to 600 °C are related to constant rearrangement of rigid plagioclase clasts narrowing quartz shear bands and affecting bulk shear stresses (Figure 3).

Additional experiments with smaller initial grain sizes (0.5 cm), without biotite, and with an initial phase distribution rotated by 90° resulted display stress evolutions without significant difference to the ones presented in the main article (see Supporting Information; Figures S1–S3 and Movies Exp37–46).

3.2 Peridotitic Mmineral Assemblage at Mantle Lithospheric Conditions

Figure 5 illustrates the textural evolution, viscosity distribution, grain sizes and deformation mechanisms of the peridotitic numerical experiments with dynamic grain-size evolution after a bulk shear strain of γ = 20. At 800 °C, the marker distribution shows pyroxene patches stretched and rotated towards the orientation of shearing, resembling elongate sigmoids (Figure 5a). Viscosities for both olivine and pyroxene show values of 10^{20}–10^{21} Pa·s, except along localized olivine shear bands that exhibit viscosities of between 10^{18} and 10^{19} Pa·s. After γ = 20, grain sizes are similar for olivine and pyroxene in less strained zones (~300

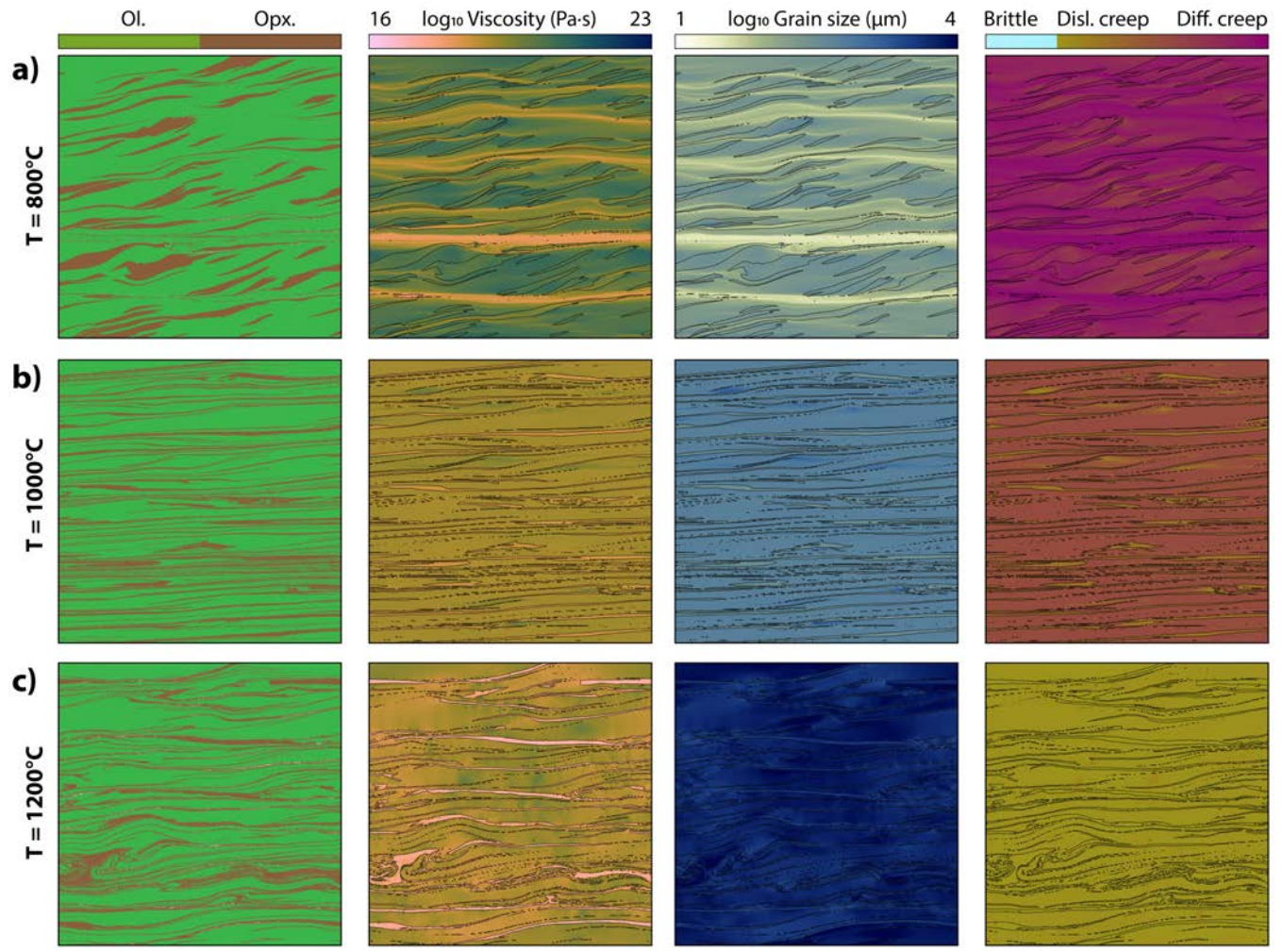

Figure 5 – Marker composition, viscosity, grain size, and deformation mechanism of numerical experiments with a mantle peridotitic mineral assemblage after shear strain of γ =10. **a)** 800 °C, **b)** 1000 °C, and **c)** 1200 °C.

μm), whereas olivine grain sizes in localized shear bands display values of as low as 30 μm. The dominant deformation mechanism of both olivine and pyroxene is diffusion creep, with dislocation creep acting in parallel for olivine in less strained zones (Figure 5a).

At a temperature of 1000 °C, pyroxene domains are stretched parallel to the shear direction across the entire model domain (Figure 5b). In some locations, asymmetric folds develop, representing the general shear sense. Viscosities of olivine and pyroxene exhibit values of ~10^{19} and ~10^{18} Pa·s, respectively. Pyroxene develops lower-viscosity shear bands throughout the experiment. Grain sizes of pyroxene are similar to the experiment at 800 °C (~300 μm), while olivine shows slightly increased grain sizes of ~600 μm. Elongated pyroxene domains predominantly deform by dislocation creep (Figure 5b). Olivine shows a deformation mechanism composed of both dislocation and diffusion creep, with dislocation creep dominating in patches of larger grain size.

At 1200 °C, pyroxene domains develop intense folding and rotational structures, in contrast to the linear shear band geometries observed at 1000 °C (Figure 5c). Viscosity of olivine is ~10^{19}–10^{20} Pa·s, while the viscosity of pyroxene is significantly lower, at values of ~10^{17} Pa·s. Olivine grain sizes are ~5 mm, while grain sizes in low-viscosity pyroxene domains are in the range of 2 mm (Figure 5c). In contrast to experiments at 1000 °C, both olivine and pyroxene deform predominantly by dislocation creep, with a few small areas where diffusion creep is active in olivine correlating with smaller grain sizes (Figure 5c).

The evolution of the average olivine and pyroxene grain sizes during shearing again strongly depends on the temperature conditions (Figure 6a,b). Brittle-plastic failure dominates for the experiments at 500 and 600 °C in both olivine and pyroxene. Therefore, changes in grain sizes are not recorded (Figure 6; Supplementary Movies in Supporting Information). At temperatures between 700-900 °C for olivine and 700-1000 °C for pyroxene, there is an initially steep decrease, approximately linear with shear strain, in grain size followed by a sharp transition between 1.5 < γ < 3, where the grain size either reaches an equilibrium grain size or steadily continues to decrease over the remainder of the experiment (Figure 6a,b). At temperatures between 1000-1100 °C for olivine and 1100 °C for pyroxene,

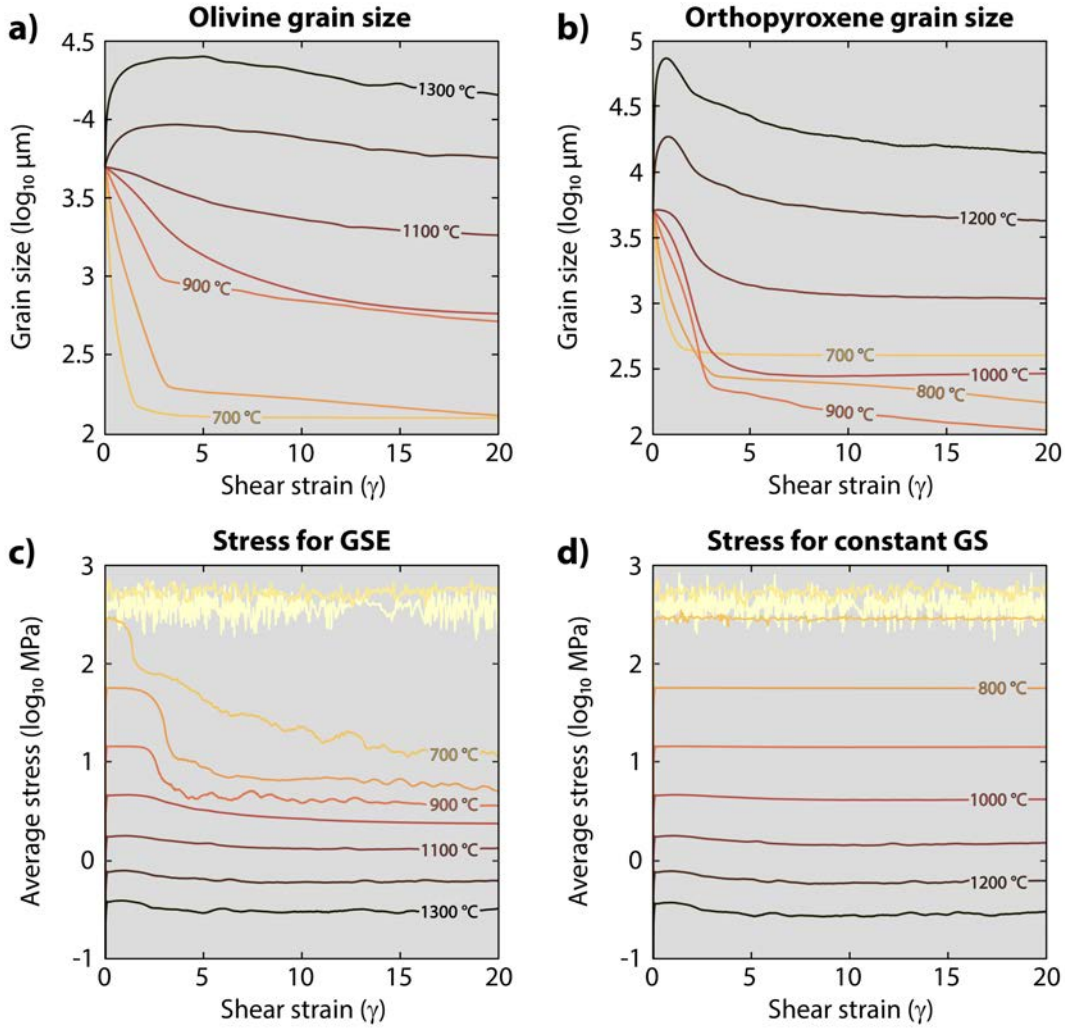

Figure 6 – Temporal evolution of grain-size and stress for mantle peridotitic experiments. **(a)** Olivine and **(b)** orthopyroxene grain size for experiments with dynamic grain size evolution. Average stress for **(c)** experiments with dynamic grain-size evolution and for **(d)** experiments with constant grain size.

the grain size decreases at a slower rate reaching equilibrium grain sizes by γ = 20 (Figure 6a,b). At temperatures of 1200-1300 °C for both olivine and pyroxene, there is an initial stage of grain growth followed by grain size reduction (related to the strain-dependent increase of λ) to values larger than the initial 5 mm, with pyroxene showing a faster rate of grain-size reduction relative to olivine (Figure 6a,b). In the peridotitic experiments, only those at 700, 1000, and 1100 °C reach an equilibrium grain size in both olivine and pyroxene by γ = 20 (Figure 6a,b).

The evolution of average stresses for olivine-pyroxene experiments with dynamic grain-size evolution develop peak stresses after initial elastic loading between ~0.3 MPa at 1300 °C and ~400 MPa at 500 and 600 °C (Figure 6c). Average stress values stabilize towards long-term values, but with significant strength loss at intermediate temperatures of 700–900 °C (Figure 6c). Intense fluctuation of stress is observed at 500 and 600 °C as a result of brittle-plastic deformation. Stress evolution of experiments with constant grain sizes show that average stresses remain roughly at initial peak values without considerable weakening during shearing (Figure 6d). Similar to the grain-size evolution experiments, fluctuations in stress related to brittle failure are observed at temperatures up to 700 °C.

4 Discussion

4.1 Comparison to Natural Shear Zones

Numerical shear experiments of granitoid and peridotitic rocks with initial mineral distributions constrained from hand specimens reproduce first-order textural features observed in mylonitic shear zones. At low temperatures (350–500 °C), the granitoid experiments show the rheological interplay between plagioclase deforming by brittle processes and quartz deforming by ductile/viscous processes, similar to many mid-crustal shear zones (e.g., *Viegas et al.*, 2016). This rheological contrast implies that strain accumulates preferentially within quartz, while plagioclase forms clasts with increased rigidity, typical for granitoid mylonitic shear zones (e.g., *Trouw et al.*, 2009). For the peridotitic assemblage, numerical experiment textures at

low temperature (≤600 °C) are defined by brittle deformation of both olivine and pyroxene, similar to natural observations (*Warren and Hirth*, 2006). At intermediate temperatures, pyroxene patches form elongated and flattened sigmoidal clasts, while at higher temperatures, they stretch to become weak inclusions (Figure 5). Such a flattening and stretching of pyroxene grains has been reported from natural peridotitic mylonites (*Dijkstra et al.*, 2004; *Jaroslow et al.*, 1996; *Vissers et al.*, 1995), while laboratory experiments support the observation that orthopyroxene may become weaker than olivine at lithospheric conditions above 800 °C (*Ohuchi et al.*, 2011).

The grain sizes obtained for quartz and plagioclase (Figure 4a,b) as well as for olivine and pyroxene (Figure 6a,b) are consistent with grain sizes from naturally deformed granitoid crustal rocks (*Behr and Platt*, 2011; *Dong et al.*, 2019; *Speciale et al.*, 2022) and mantle peridotites (*Dygert et al.*, 2019; *Hansen and Warren*, 2015), respectively. Grain-size reduction in numerical experiments occurs at bulk shear strains below ~10 for quartz, and below ~5 for olivine and pyroxene, reflected by a synchronous reduction in bulk strength, while plagioclase grain size reduces at a slower rate (Figure 4, 6). For quartz, experiments at lower temperatures require larger bulk shear strain to achieve constant grain sizes due to the slower development of a foliated texture (Figure 4a). The slow grain-size reduction in plagioclase is due to the limited amount of strain accumulated within strong clasts, hampering an increase of λ. This observation is consistent with the model proposed by *Kidder et al.* (2016) for the evolution of λ between porphyroclasts and recrystallized grains.

4.2 Deformation Mechanisms during Shearing

Deformation mechanism maps based on the implemented flow laws (see Table 1) outline the fields in which dislocation and diffusion creep, respectively, act as the dominant deformation mechanism at the modelled bulk strain rate for the granitoid (Figure 7) and peridotitic assemblages (Figure 8). Stresses and grain sizes on markers are averaged for each mineral phase after a bulk shear strain of γ = 20 and plotted onto the deformation mechanism maps. Piezometric relationships are also plotted for quartz and feldspar (Figure 7), and olivine and pyroxene (Figure 8) for comparison.

4.2.1 Granitoid Mineral Assemblage

The average grain sizes and stresses stored on quartz markers indicate that the dominant deformation mechanism is dislocation creep at all tested temperatures, as expected from the deformation mechanism map (Figure 7a). This is consistent with quartz microstructures from natural mylonites (e.g., *Stipp et al.*, 2002), as well as laboratory experiments (*Hirth and Tullis*, 1992; *Stipp and Tullis*, 2003). Numerical data for quartz shows that most of the markers accumulated strain of ε > 3 (circles in Figure 7a), with the experiment at 500 °C exhibiting the lowest percentage of such markers at 71%, related to a less strained upper part of the sheared domain (Figure 3b). Results display lower stresses and larger grain sizes for increasing temperature and are in general agreement with the experimentally-derived quartz recrystallized grain-size piezometer (*Stipp and Tullis*, 2003). However, this fit is to a certain degree imposed as the parameters used in the grain-size evolution of quartz were calibrated using the same experiments to determine the *Stipp and Tullis* (2003) piezometer (*Tokle and Hirth*, 2021). The quartz stress-grain size data points deviate from the strain-rate curves for the respective temperature (Figure 7a), given that quartz represents the interconnected weak phase in the granitoid numerical shear experiments and the bulk strain rate is locally exceeded due to the complex multi-phase texture (Figure 3).

Grain-size and stress data of anorthite at γ = 20 display a more complex picture. At 350 and 400 °C, stresses in anorthite are capped by the brittle yield strength (horizontal dashed line), as observed in the deformation mechanism plot (Figure 3a), and are therefore not shown in Figure 7b. The mean stresses and grain sizes of experiments above 400 °C all plot in the dislocation creep field (squares in Figure 7b). With increasing temperature, these data points (squares) indicate a trajectory aimed towards the field boundary line (e.g., *De Bresser et al.*, 2001) or the recrystallized grain-size piezometer (*Speciale et al.*, 2022), which plots within the diffusion creep field for the applied bulk strain rate (Figure 7b; blue line). The misfit of the data points representing all mean values, independent of strain (squares), and the piezometer can be explained by the percentage of plagioclase markers that experienced strain of ε > 3, which here is considered necessary for representing full recrystallization. At 450 °C, all plagioclase markers show low accumulated strain (0% with ε > 3). The percentage of recrystallized plagioclase increases with temperature to a value of 50% at 750 °C (Figure 7b). Stress and grain-size data for recrystallized (ε > 3) data points are in first-order agreement with the plagioclase piezometer, however diverging farther from it at higher temperatures related to faster grain growth (circles in Figure 7b).

The overall plagioclase grain sizes represent a transient state for a partially recrystallized plus a non-strained fraction. With ongoing shearing, grain sizes will continue to decrease moving the grain-size and stress data plotted in Figure 7 towards the field boundary line and piezometer. This fits with laboratory experiments (*Rybacki and Dresen*, 2004) and natural examples (*Tullis et al.*, 1996). At a certain stage, further grain-size reduction beyond the field boundary line will be hampered once diffusion creep becomes the dominant deformation mechanism, as suggested by *De Bresser et al.* (2001).

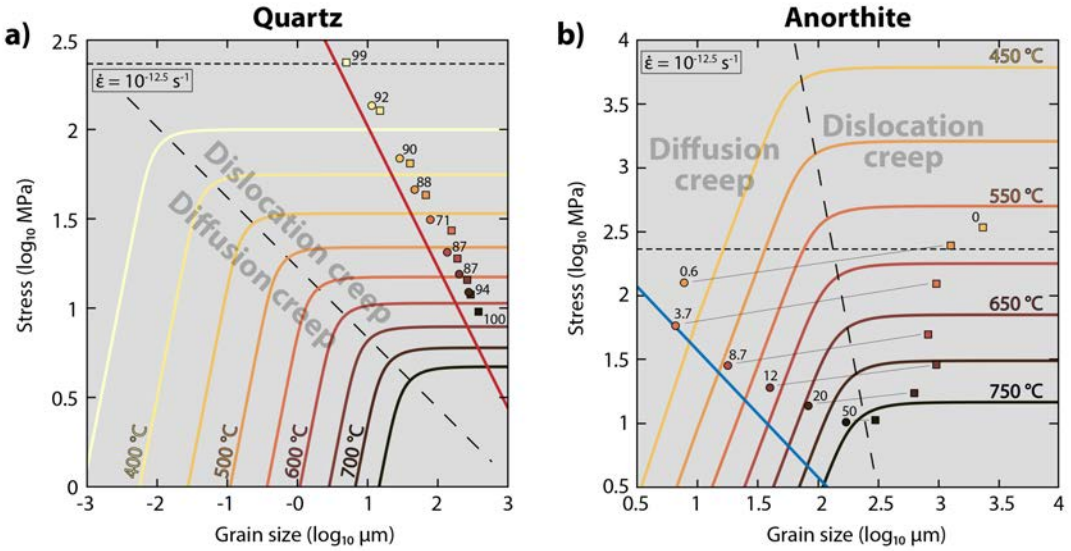

Figure 7 – Deformation mechanism maps for **(a)** quartz and **(b)** anorthite for a strain rate of $10^{-12.5}$ s^{-1}. See Table 1 for rheological parameters. Horizontal dashed line: Brittle yield strength at 371 MPa confining pressure. Field boundaries indicated by long dashed lines. Squares indicate mean marker grain size and stress after bulk shear strain of $\gamma = 20$. Circles indicate mean marker grain size and stress for markers with accumulated strain $\varepsilon > 3$, the number indicates the percentage of markers that exceeds strain $\varepsilon > 3$. Thin straight lines connecting circles and squared in (b) indicate same temperature experiments for better readability. Red line in (a): Quartz piezometer (*Stipp and Tullis*, 2003). Blue line in (b): Feldspar piezometer (*Speciale et al.*, 2022).

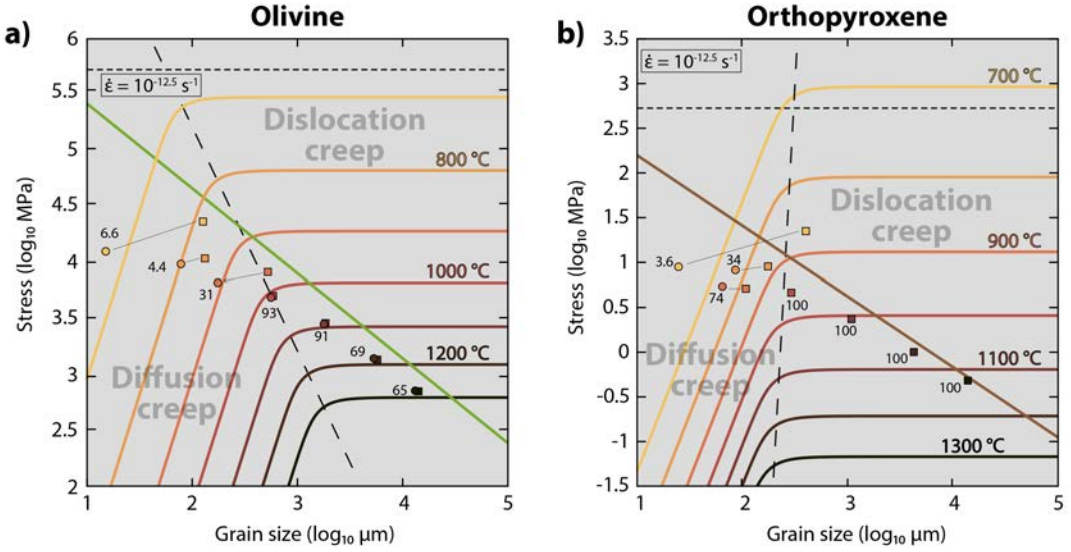

Figure 8 – Deformation mechanism maps for **(a)** olivine and **(b)** orthopyroxene for a strain rate of $10^{-12.5}$ s^{-1}. See Table 1 for rheological parameters. Horizontal dashed line: Brittle yield strength at 530 MPa confining pressure. Field boundaries indicated by long dashed lines. Squares indicate mean marker grain size and stress after shear strain of $\gamma = 20$. Circles indicate mean marker grain size and stress for markers with accumulated strain $\varepsilon > 3$, the number indicates the percentage of markers that exceeds strain $\varepsilon > 3$. Thin straight lines connecting circles and squared indicate same temperature experiments for better readability. Green line in (a): Olivine piezometer (*Van der Wal et al.*, 1993). Brown line in (b): Pyroxene piezometer (*Speciale et al.*, 2022).

4.2.2 Peridotitic Mineral Assemblage

Experiments at 500 and 600 °C deform dominantly by brittle failure (Figure 5a) capping stresses depending on frictional properties (Figure 8a; dashed line) and are therefore ignored. For experiments above 600 °C, the average olivine grain sizes and stresses after a bulk shear strain of $\gamma = 20$ illustrate that dislocation creep is the dominant deformation mechanism above 1000 °C, while diffusion creep prevails at lower temperatures (Figure 8a). Similar to the granitoid mineral phases, squares indicate the mean marker data, while circles represent only markers with an accumulated strain of $\varepsilon > 3$. The olivine grain-size piezometer (*Van der Wal et al.*, 1993) shows a good fit for experiments where dislocation creep dominates deformation (Figure 8a). Minor deviation from the piezometer occurs when conditions approach the field boundary line and into the diffusion creep field (Figure 8a; T < 1000 °C). There, grain sizes of

markers with strain ε < 3 (circles) constitute a lesser percentage, but plot deeper into the diffusion creep field.

The observation that olivine switches from dislocation creep to diffusion creep related to grain-size reduction during lithospheric shear zone formation is in agreement with natural (*Dygert et al.*, 2019), experimental (*Linckens et al.*, 2015) and numerical studies (*Ruh et al.*, 2022). However, our results also demonstrate that dislocation creep remains the dominant deformation mechanism of high-strain shear zones for temperatures above 1000 °C, as a result of faster grain growth and therefore larger grain sizes, hampering the activation of diffusion creep (e.g., *De Bresser et al.*, 2001). This underlines the importance of a sophisticated grain-size-evolution model when using composite flow laws in contrast to constant grain sizes, which would rather result in shallow dislocation creep and deep diffusion creep of the mantle (*Liao et al.*, 2017).

Grain-size and stress data of orthopyroxene shows a similar distribution as olivine, with low-temperature experiments in the small grain size diffusion creep field and experiments above 1000 °C plotting in the dislocation creep field, aligning along the piezometer (*Speciale et al.*, 2022), which is adapted from the experimentally-derived olivine piezometer (Figure 8b). Strain-dependent data shows that the percentage of markers with an accumulated strain of ε > 3 increases from ~4 to 100% between 700 to 1000 °C, similar to olivine (Figure 8), which indicates highly localized deformation at low temperatures.

Based on experimental data from *Lawlis* (1998) and *Bruijn and Skemer* (2014) proposed that the transition from diffusion to dislocation creep of orthopyroxene occurs at grain sizes between 150–500 µm, which is in agreement with the flow laws applied here. Grain-size reduction by dynamic recrystallization at intermediate lithospheric temperatures (~700 °C) and consequent activation of diffusion creep in orthopyroxene, similar to our results (Figure 5b), has furthermore been reported from natural examples of mantle shear zones from the Hilti massif in Oman (*Linckens et al.*, 2011).

4.3 Grain-size-sensitive Weakening in Granitoid and Peridotitic Shear Zones

To quantify the effect of grain-size reduction and the consequent transition from dislocation to diffusion creep for the weakening and thus localization of ductile shear zones in crustal and mantle rocks, we considered the bulk stress evolution of numerical experiments with a grain-size-evolution model (Figure 4c and 6c) and with a constant grain size (Figures 4d and 6d). Weakening of each experiment is quantified by dividing the residual stress, i.e. the long-term stress (γ = 15–20), by the peak stress (Figure 9).

For granitoid experiments with constant grain size of 2 cm, dislocation creep is the dominant deformation mechanism (Figure 7; outside of illustrated domain) and weakening is thus a result of textural reorganization and interconnection of weak phases during shearing. Purely textural weakening of ~55% occurs at 550 °C (Figure 9a; circles), where the difference in strength between quartz and anorthite is largest (Figure 1a) and texture is thus most important, as previously pointed out in laboratory experiments (*Holyoke and Tullis*, 2006). At low temperatures, anorthite strength is defined by the brittle yield envelope and at higher temperatures, dislocation creep strength of quartz and anorthite converge (Figure 1a), resulting in nearly-isoviscous shear (Figure 3c). For the grain-size evolution model suite, additional weakening related to grain-size reduction occurs due to the activation of diffusion creep as the dominant deformation mechanism for anorthite (Figure 7b; squares). At 350 and 400 °C, anorthite strength is limited by brittle yield and no grain-size-induced weakening occurs. For temperatures above 500 °C, additional grain-size-induced weakening is ~15%, thus is secondary to textural weakening in this case, but still represents an important component in the initiation of granitoid crustal shear zones (Figure 9a).

For peridotitic experiments, a constant grain size of 5 mm lies in the dislocation creep field for both olivine and orthopyroxene (Figure 8). Weakening in constant grain size experiments is thus purely related to their textural evolution. Experiments below 1000 °C show a weakening of only a few percent, while above this temperature, a linear increase of weakening reaches up to 30% loss of strength for the experiment at 1300 °C (Figure 9b; circles). This onset of textural weakening at higher temperatures reflects the strength contrast of implemented olivine and pyroxene flow laws, where at 1300 °C, dislocation creep of pyroxene is roughly one order of magnitude weaker than olivine (Figure 1d). Given that pyroxene initially appears as isolated patches (Figure 1f), their elongation and eventual connection facilitates shearing, in case they represent the weak phase (Figure 5b, c). These observations fit earlier models, which showed that only weak inclusions lead to textural weakening if sheared (*Rast and Ruh*, 2021). If grain-size evolution is activated, weakening of experiments with a peridotitic assemblage display a strong dependence on temperature (Figure 9b; squares). At 500 and 600 °C, stresses depend on brittle strength and therefore show no difference to experiments with constant grain size. At 700 °C, grain-size-related weakening increases to >90%. Towards higher temperatures, weakening is reduced to ~30% at 1100 °C. At 1300 °C, the amount of weakening of the experiment with grain-size evolution is less than for constant grain size (Figure 9b), due to an overall increase of grain size at these temperatures compared to the initial grain size (Figure 6a,b). The intense reduction of strength

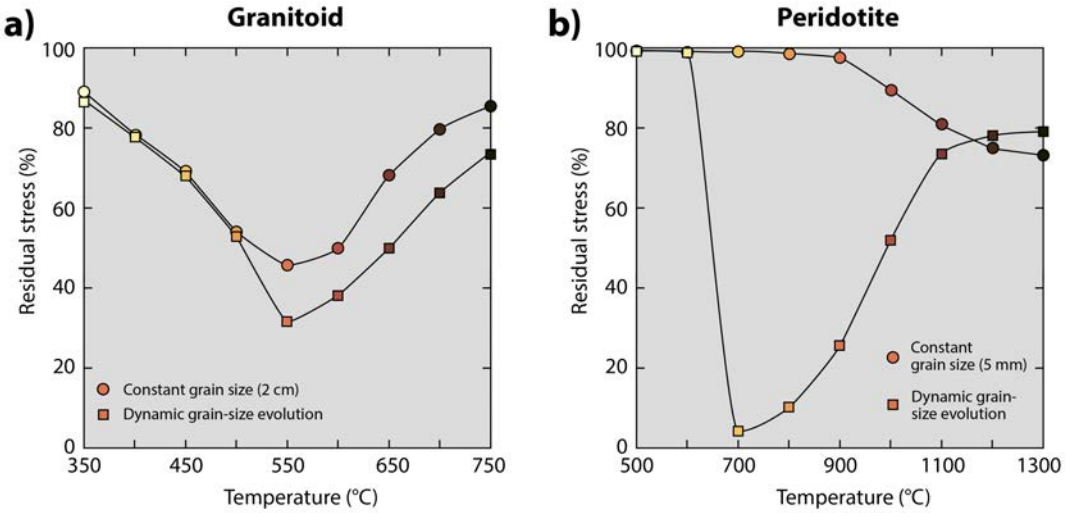

Figure 9 – Purely textural versus both textural and grain-size-sensitive weakening. **a)** Residual strength (average stress for γ = 15–20) relative to peak stress for granitoid experiments at different temperatures (see Figure 4c,d). Circles: Constant grain size. Squares: Dynamic grain-size evolution. **b)** Residual strength (average stress for γ = 15–20) relative to peak stress for peridotitic experiments at different temperatures (see Figure 6c,d). Circles: Constant grain size. Squares: Dynamic grain-size evolution.

related to rapid grain-size reduction of olivine and its importance in enhancing tectonic processes has been previously suggested (*Behn et al.*, 2009; *Warren and Hirth*, 2006). However, the presented results demonstrate that intense weakening related to grain-size reduction occurs only for temperatures up to ~1000 °C at the applied strain rate, which may help explain the downward widening of natural lithospheric mantle.

4.4 Comparison of Polyphase Models to Deformation Mechanism Maps and 1-Dimensional Solutions

The two-dimensional polyphase numerical experiments conducted here reproduce complex textures and phase mixing, each of which can affect both the grain size evolution and shear zone strength (e.g., *Montési*, 2013; *Rast and Ruh*, 2021). To understand how important these components are to estimates of shear zone weakening, we can compare our results to single-phase deformation mechanism maps and one-dimensional grain size evolution models. A comparison of granitoid shear experiments to one-dimensional models is not attempted because i) deformation of quartz is defined by dislocation creep and no grain-size-related weakening is expected (Figure 7a), consistent with quartz single-phase deformation mechanism maps, and ii) plagioclase behaves mostly as rigid clasts in two-dimensional experiments (Figure 3) and most plagioclase markers exhibit low strain (ε < 3) indicating out-of-equilibrium grain sizes (Figure 7b). A more meaningful comparison is attempted here for the peridotitic system with olivine and pyroxene (Figure 10). *Rutter and Brodie* (1988) suggested that in natural shear zones, deformation in the dislocation creep regime produces recrystallized grains that follow the piezometric relationship for phases and conditions in which the piezometer lies in the diffusion creep field. The resulting weakening can be roughly estimated from a deformation mechanism map (e.g., Figure 10a). Figure 8 demonstrates that although stresses are lower in the recrystallized grains (circles) that fall in the diffusion creep field (experiments at 700–900 °C), they are not as low as would be expected from the deformation mechanism map (e.g., Figure 10a), likely because strain rates vary throughout the aggregate. Hence, deformation mechanism maps seem to provide good proxies for the conditions of weakening, but may not provide accurate estimates of weakening magnitudes.

Additionally, a one-dimensional stress and grain-size evolution model of single-phase olivine and pyroxene at a constant strain rate of 10 $s^{-12.5}$ s^{-1} allows to calculate the expected stress loss with increasing shear strain. Both olivine and pyroxene stress curves indicate significant stress loss after a shear strain of γ = 20 at temperatures below 1000 °C, while at higher temperatures stresses remain roughly constant (Figure 10b,c). The resulting percentage of stress loss, or the residual stress, of both individual phases for the piezometric and GSE constraints hence show intense weakening for lower temperatures (700–900 °C), while no stress loss results above 1100 °C. Such characteristics are similar to our two-dimensional shear experiments (Figure 10d). Particularly olivine displays an excellent fit of 1D and 2D stress data, indicating that texture-related effects may be neglected for peridotitic assemblages and that pure olivine rheology represents a good approximation to model mantle deformation.

On the other hand, the rheological difference between quartz and anorthite (Fig. 1c), and the fact that quartz never reached the diffusion creep field

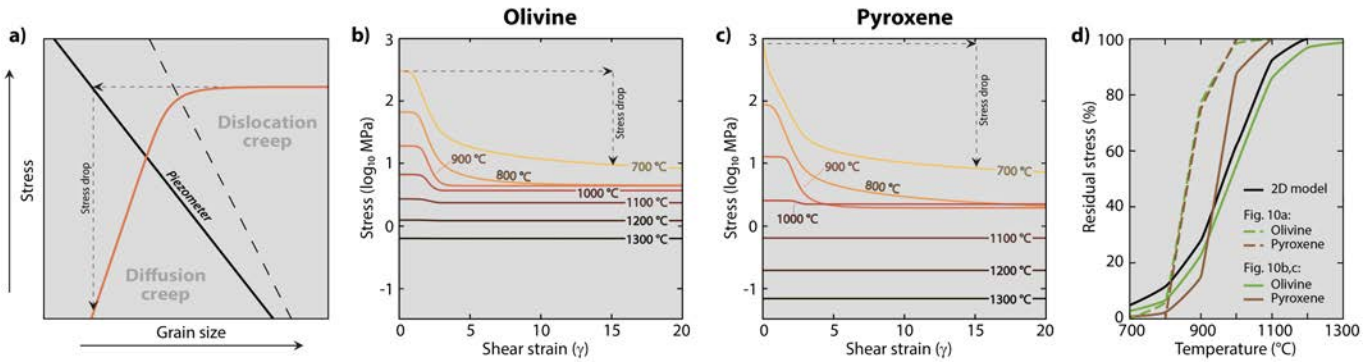

Figure 10 – Comparison of two-dimensional peridotite experiments to one-dimensional estimations for strength reduction related to grain-size reduction. **a)** Schematic deformation mechanism map for constant temperature and strain rate. Dashed line: Deformation mechanism boundary. Black line: Schematic piezometer. Dashed arrows: Expected weakening effects related to dynamic recrystallization (after *Rutter and Brodie*, 1988). Not to scale. **b)** and **c)** One-dimensional evolution of stress for individual mineral phases applying the same flow laws and grain-size evolution parameters as in two-dimensional experiments (Table 1) and a constant strain rate of $10^{-12.5}$ s^{-1} for olivine (b) and pyroxene (c). Dashed arrows indicate the resulting grain-size-related stress reduction. **d)** Grain-size-related stress reduction of one- and two-dimensional experiments at different temperatures. Black line: Grain-size-dependent fraction of two-dimensional experiments (Figure 9b). Dashed coloured lines: Analytical stress loss based on piezometer relationship shown in (a) for olivine (green) and pyroxene (brown). Full coloured lines: Residual stress (stress after $\gamma = 20$ divided by maximal stress) of one-dimensional GSE experiments shown in (b; olivine) and (c; pyroxene).

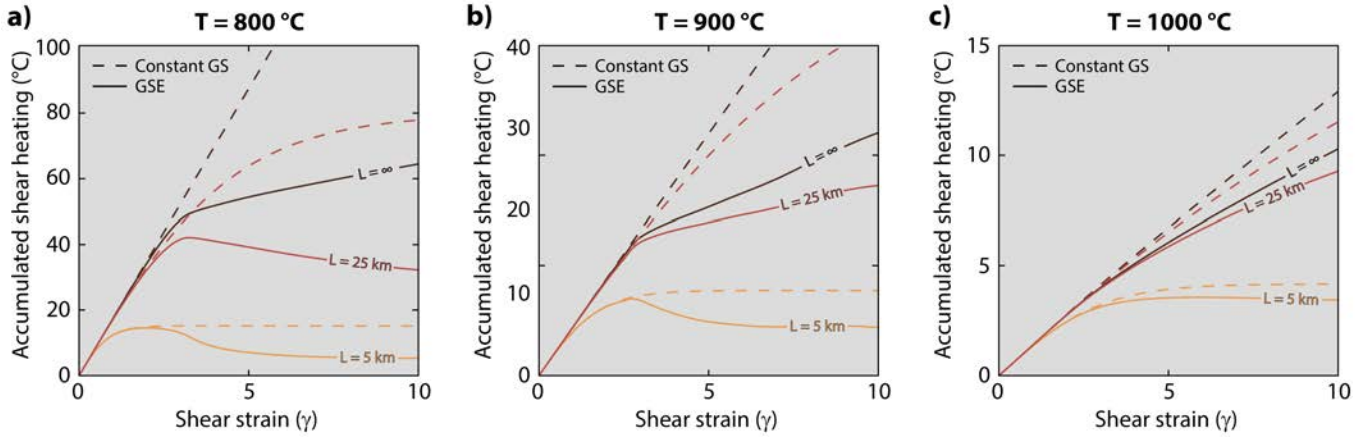

Figure 11 – Heat produced by shear heating for peridotitic numerical experiments at **(a)** 800 °C, **(b)** 900 °C, and **(c)** 1000 °C. Full lines: experiments with grain-size evolution. Dashed lines: experiments with constant grain size. Dark color: no diffusive heat loss, i.e. infinitive shear zone with. Red color: diffusive heat loss with a shear zone width of L = 25 km. Orange color: diffusive heat loss with a shear zone width of L = 5 km.

(Figure 7a), nullify a comparison to one-dimensional models. Intense grain-size reduction of anorthite along the rims of larger clasts (Figure 3b) and intensely stretched shear-parallel bands (Figure 3c) demonstrate the interaction of texture development and grain-size evolution, underlining the importance of a two-dimensional setup for shear zones with granitoid crustal rock assemblages.

4.5 Effect of Grain-size Reduction on Viscous Shear Heating

If grain size reduces sufficiently for diffusion creep to become the dominant deformation mechanism, it is intrinsically related to a reduction in shear strength (Fig. 1a,d). Such a loss in strength whilst strain rates remain constant result in a decrease in expended work, which is defined by $\dot{W} = \sigma\dot{\varepsilon}$. In thermo-mechanical numerical models, mechanical work is often entirely transformed to heat, thus called shear heating, and as such has for example been interpreted to facilitate subduction initiation by thermal weakening of the lithosphere (e.g., *Thielmann and Kaus*, 2012). Numerical experiments presented in this study are conducted at constant temperatures and thus shear heating is ignored. However, potential heat production can be calculated by integrated energy dissipation during shearing to demonstrate and quantify the effect of grain-size reduction on shear heating. Figure 11 shows heat production by energy dissipation for peridotitic assemblages at 800, 900, and 1000 °C for constant grain sizes (dashed lines) and grain-size evolution (full lines). Peridotite experiments with and without grain-size evolution are compared because they show a large difference in long-term strength (Figure 6c,d and 9b). Shear

heating within a shear zone produces a temperature gradient with its surroundings, which undergoes thermal diffusion. Therefore, we calculated the temperature increase related to shear heating for variable shear zones widths across which heat can diffuse, here calculated by a zero-dimensional finite difference heat diffusion. After a shear strain of γ = 10, the temperature increase in case of no diffusive heat loss of the experiments with constant grain size ranges in between ~13 °C and ~200 °C, while the same experiments with grain-size evolution shows temperature increases in the order of ~10–60 °C, respectively (Figure 11, dark lines). The temperature increase related to shear heating is significantly reduced for shear zones with a width below five kilometres due to diffusive heat loss, indicating that the effect becomes insignificant for narrow shear zones such as the ones presented in this study. In general, the effect of grain-size reduction on shear heating challenges the idea that shear heating is an important factor for the localization of mantle lithospheric shear zones (*Hartz and Podladchikov*, 2008; *Kaus and Podladchikov*, 2006), given the common evidence for grain-size reduction in mantle rocks.

4.6 Limitations of the Modelling Approach

This study presents effects of grain-size evolution on mechanical weakening during shearing of granitoid and peridotitic mineral assemblages consistent with natural shear zones. While the presented study allows us to discuss these effects for a simplified shear zone, many processes may occur in natural shear zones that are ignored in the implemented numerical formulations. Simplification of the model setups with regard to processes observed in natural shear zones include:

- Natural shear zones may progressively widen or narrow during localization, depending on their strengthening or weakening potential, respectively (*Fossen and Cavalcante*, 2017). Such a geometric response results in strain rate variations with a feedback effect on grain size and ultimately the stress evolution within the shear zone, in contrast to constant width and strain rate applied in the presented experiments.
- The presented models consist of simplified mineral assemblages, given the need for both published dislocation and diffusion flow laws and grain growth laws for the applied phases (see Table 1). While flow laws are typically based on laboratory experiments scaled up to lithospheric conditions, a simplification itself, natural rocks furthermore exhibit a more complex chemical composition than reflected in the presented model setup.
- Viscous shear heating can become an important factor in the mechanical weakening of ductile shear zones (e.g., *Thielmann and Kaus*, 2012; *Hartz and Podladchikov*, 2008).The present study ignores shear heating given the small scale of modelled shear zone width and the consequent effective thermal diffusion of additional heating. Section 4.5. provides first-order constraints on accumulated heat depending on shear zone width and their dependence on grain-size reduction.
- Several studies also demonstrated that mechanisms like dissolution creep and grain-boundary sliding affect the rheologies of modelled mineral deformation (*Marti et al.*, 2018; *Warren and Hirth*, 2006), while this study only considers dislocation and diffusion creep. Relatedly, we assume for simplicity here that brittle-plastic deformation does not contribute to grain-size reduction, but cataclastic deformation may trigger grain-size-sensitive creep mechanisms in nature (*Marti et al.*, 2017; *Menegon et al.*, 2013; *Viegas et al.*, 2016).
- Minor phases may have a significant impact on strength and deformation patterns of polyphase shear experiments (e.g., *Tokle et al.*, 2023) and phase-pinning has a direct effect on grain-size evolution, which in turn affects mechanical strength (*Farla et al.*, 2013; *Linckens et al.*, 2015).
- The fraction of dissipated energy going into grain-size reduction (λ) has a strong effect on the resulting grain sizes and thus mechanical evolution, but its dependence on strain, temperature, or strain rate remains unclear. While steady state values of λ may be interpreted from laboratory experiments (e.g., *Tokle and Hirth*, 2021), its evolution during shear zone infancy at low strains has not been constrained.
- Grain-size information is stored on Lagrangian markers without geometric implications related to the evolving microstructure of the deforming numerical shear experiment, but only depends on the local thermal and mechanical marker characteristics.

Even though the above listed points may contribute to the deformation history of a natural shear zone, the geometrical and dynamic simplifications introduced in our approach do not undermine the importance of a self-consistent grain-size-evolution model for strength and strain localization in the lithosphere.

5 Conclusions

Two-dimensional numerical shear experiments of granitoid and peridotitic compositions are able to reproduce textural features typically observed in natural shear zones and reveal that grain-size and stress evolution of individual mineral phases are well constrained with published piezometers. The presented numerical experiments demonstrate that weakening during localization of crustal and mantle

lithospheric shear zones is a combined effect of textural and grain-size evolution. For felsic crustal mineral assemblages, weakening may reach ~80% of weakening at 550 °C, mainly based on the formation of shear-parallel layering, with secondary influence of grain size reduction. At higher temperatures, textural weakening reduces due to converging viscous strength of quartz and plagioclase. For peridotitic mantle rocks, olivine is much more abundant than pyroxene, which in turn has a minor geometric effect during shear zone localization. However, grain-size reduction of olivine below temperatures of ~1000 °C results in intense weakening (>90%) of the initial rock strength. The amount of weakening in peridotitic rocks induced by grain-size reduction of olivine is shown to be well constrained by one-dimensional models, while for granitoitic assemblages, two-dimensional models are necessary to capture textural complexities and their effect on stress, strain rate, and grain size. The findings underline the importance of grain-size reduction and the consequent activation of grain-size-sensitive rheologies for the weakening of ductile shear zones during initial strain localization, especially in the mantle lithosphere, and provides quantitative constraints that improve our understanding of long-term lithospheric strength.

Acknowledgements

The authors thank the two reviewers, the Associate Editor, and the Editor for their constructive comments that improved the quality of the manuscript. This work was partly supported by a Ramón y Cajal scholarship (RYC2021-031331-I) funded by the Spanish Ministry of Science and Innovation.

Author contributions

J.B.R. wrote the numerical code, conducted and interpreted the experiments and wrote the manuscript. **W.M.B.** contributed to the conception and design of the study and substantially revised it. **L.T.** investigated experimental data to infer crucial parameters, interpreted the data and revised the manuscript.

Data availability

All modelling was conducted with the numerical code "Norma". One- and two-dimensional examples are available in the Supporting Information at https://doi.org/10.3929/ethz-b-000657113. Additional granitoid experiments with different initial grain size, without biotite, and with rotated initial phase distribution, together with movies of all numerical experiments, are available in AVI format in the Supporting Information at https://doi.org/10.3929/ethz-b-000657113.

Competing interests

The authors declare no competing interests.

Peer review

This publication was peer-reviewed by Melanie Finch and an anonymous reviewer. The full peer-review report can be found here: tektonika.online/index.php/home/article/view/68/79

Copyright notice

References

Austin, N. J., and B. Evans (2007), Paleowattmeters: A scaling relation for dynamically recrystallized grain size, *Geology*, *35*(4), 343–346, doi: 10.1130/G23244A.1.

Behn, M. D., G. Hirth, and J. R. Elsenbeck, II (2009), Implications of grain size evolution on the seismic structure of the oceanic upper mantle, *Earth and planetary science letters*, *282*(1-4), 178–189, doi: 10.1016/j.epsl.2009.03.014.

Behr, W. M., and J. P. Platt (2011), A naturally constrained stress profile through the middle crust in an extensional terrane, *Earth and planetary science letters*, *303*(3-4), 181–192, doi: 10.1016/j.epsl.2010.11.044.

Bercovici, D. (2003), The generation of plate tectonics from mantle convection, *Earth and planetary science letters*, *205*(3-4), 107–121, doi: 10.1016/s0012-821x(02)01009-9.

Bercovici, D., Y. Ricard, and G. Schubert (2001), A two-phase model for compaction and damage: 1. general theory, *Journal of geophysical research*, *106*(B5), 8887–8906, doi: 10.1029/2000jb900430.

Braun, J., J. Chéry, A. Poliakov, D. Mainprice, A. Vauchez, A. Tomassi, and M. Daignières (1999), A simple parameterization of strain localization in the ductile regime due to grain size reduction: A case study for olivine, *Journal of geophysical research*, *104*(B11), 25,167–25,181, doi: 10.1029/1999jb900214.

Brodie, K. H., and E. H. Rutter (2000), Deformation mechanisms and rheology: why marble is weaker than quartzite, *Journal of the Geological Society*, *157*(6), 1093–1096, doi: 10.1144/jgs.157.6.1093.

Bruijn, R. H., and P. Skemer (2014), Grain-size sensitive rheology of orthopyroxene, *Geophysical research letters*, *41*(14), 4894–4903, doi: 10.1002/2014GL060607.

Bystricky, M., K. Kunze, L. Burlini, and J. Burg (2000), High shear strain of olivine aggregates: rheological and seismic consequences, *Science*, *290*(5496), 1564–1567, doi: 10.1126/science.290.5496.1564.

Ceccato, A., L. Menegon, G. Pennacchioni, and L. F. G. Morales (2018), Myrmekite and strain weakening in granitoid mylonites, *Solid earth*, *9*(6), 1399–1419, doi: 10.5194/se-9-1399-2018.

Cross, A. J., and P. Skemer (2019), Rates of dynamic recrystallization in geologic materials, *Journal of Geophysical Research-Solid Earth*, *124*(2), 1324–1342, doi: 10.1029/2018JB016201.

Dabrowski, M., D. W. Schmid, and Y. Y. Podladchikov (2012), A two-phase composite in simple shear: Effective mechanical anisotropy development and localization potential, *Journal of Geophysical Research, [Solid Earth]*, *117*.

Dannberg, J., Z. Eilon, U. Faul, R. Gassmöller, P. Moulik, and R. Myhill (2017), The importance of grain size to mantle dynamics and seismological observations, *Geochemistry, Geophysics, Geosystems*, *18*(8), 3034–3061, doi: 10.1002/2017gc006944.

De Bresser, J. H. P., J. H. Ter Heege, and C. J. Spiers (2001), Grain size reduction by dynamic recrystallization: can it result in major theological weakening?, *Geologische Rundschau: Zeitschrift fur allgemeine Geologie*, *90*(1), 28–45.

Dijkstra, A. H., M. R. Drury, R. L. M. Vissers, J. Newman, and H. L. M. Van Roermund (2004), Shear zones in the upper mantle: evidence from alpine- and ophiolite-type peridotite massifs, *Flow Processes in Faults and Shear Zones*, *224*, 11–24, doi: Doi 10.1144/Gsl.Sp.2004.224.01.02.

Dong, Y., S. Cao, X. Cheng, J. Liu, and H. Cao (2019), Grain-size reduction of feldspar and flow of deformed granites within the gaoligong shear zone, southwestern yunnan, china, *SCIENCE CHINA Earth Sciences*, *62*(9), 1379–1398, doi: 10.1007/s11430-018-9351-8.

Dresen, G., Z. Wang, and Q. Bai (1996), Kinetics of grain growth in anorthite, *Tectonophysics*, *258*(1-4), 251–262, doi: 10.1016/0040-1951(95)00203-0.

Duretz, T., S. M. Schmalholz, and Y. Y. Podladchikov (2015), Shear heating-induced strain localization across the scales, *Philosophical Magazine A*, *95*(28-30), 3192–3207, doi: 10.1080/14786435.2015.1054327.

Dygert, N., R. E. Bernard, and W. M. Behr (2019), Great basin mantle xenoliths record active lithospheric downwelling beneath central nevada, *Geochemistry, Geophysics, Geosystems*, *20*(2), 751–772, doi: 10.1029/2018gc007834.

Farla, R. J. M., S.-I. Karato, and Z. Cai (2013), Role of orthopyroxene in rheological weakening of the lithosphere via dynamic recrystallization, *Proceedings of the National Academy of Sciences of the United States of America*, *110*(41), 16,355–16,360, doi: 10.1073/pnas.1218335110.

Finch, M. A., P. D. Bons, F. Steinbach, A. Griera, M. G. Llorens, E. Gomez-Rivas, H. Ran, and T. de Riese (2020), The ephemeral development of c' shear bands: A numerical modelling approach, *Journal of Structural Geology*, *139*.

Fossen, H., and G. C. G. Cavalcante (2017), Shear zones – a review, *Earth-science reviews*, *171*, 434–455, doi: 10.1016/j.earscirev.2017.05.002.

Fuchs, L., and T. W. Becker (2019), Role of strain-dependent weakening memory on the style of mantle convection and plate boundary stability, *Geophysical Journal International*, *218*(1), 601–618, doi: 10.1093/gji/ggz167.

Gerya, T. V., D. Bercovici, and T. W. Becker (2021), Dynamic slab segmentation due to brittle-ductile damage in the outer rise, *Nature*, *599*(7884), 245–250, doi: 10.1038/s41586-021-03937-x.

Goncalves, P., E. Oliot, D. Marquer, and J. A. D. Connolly (2012), Role of chemical processes on shear zone formation: an example from the grimsel metagranodiorite (aar massif, central alps), *Journal of Metamorphic Geology*, *30*(7), 703–722, doi: 10.1111/j.1525-1314.2012.00991.x.

Hansen, L. N., and J. M. Warren (2015), Quantifying the effect of pyroxene on deformation of peridotite in a natural shear zone, *Journal of Geophysical Research, [Solid Earth]*, *120*(4), 2717–2738.

Hartz, E. H., and Y. Y. Podladchikov (2008), Toasting the jelly sandwich: The effect of shear heating on lithospheric geotherms and strength, *Geology*, *36*(4), 331–334, doi: 10.1130/G24424A.1.

Heilbronner, R., and J. Tullis (2006), Evolution of c axis pole figures and grain size during dynamic recrystallization: Results from experimentally sheared quartzite, *Journal of geophysical research*, *111*(B10), doi: 10.1029/2005JB004194.

Herwegh, M., T. Poulet, A. Karrech, and K. Regenauer-Lieb (2014), From transient to steady state deformation and grain size: A thermodynamic approach using elasto-visco-plastic numerical modeling, *Journal of Geophysical Research, [Solid Earth]*, *119*(2), 900–918, doi: 10.1002/2013jb010701.

Hirth, G., and D. Kohlstedt (2003), Rheology of the upper mantle and the mantle wedge: A view from the experimentalists, *Geophysical monograph*, *138*, 83–106.

Hirth, G., and J. Tullis (1992), Dislocation creep regimes in quartz aggregates, *Journal of Structural Geology*, *14*(2), 145–159, doi: 10.1016/0191-8141(92)90053-Y.

Holyoke, C. W., III, and J. Tullis (2006), Mechanisms of weak phase interconnection and the effects of phase strength contrast on fabric development, *Journal of Structural Geology*, *28*(4), 621–640, doi: 10.1016/j.jsg.2006.01.008.

Hopper, J., and W. Buck (1993), The initiation of rifting at constant tectonic force: Role of diffusion creep, *Journal of geophysical research*, *98*(B9), 16,213–16,221, doi: 10.1029/93JB01725.

Jaroslow, G. E., G. Hirth, and H. J. B. Dick (1996), Abyssal peridotite mylonites: implications for grain-size sensitive flow and strain localization in the oceanic lithosphere, *Tectonophysics*, *256*(1-4), 17–37, doi: 10.1016/0040-1951(95)00163-8.

Ji, S., Z. Jiang, E. Rybacki, R. Wirth, D. Prior, and B. Xia (2004), Strain softening and microstructural evolution of anorthite aggregates and quartz–anorthite layered composites deformed in torsion, *Earth and planetary science letters*, *222*(2), 377–390, doi: 10.1016/j.epsl.2004.03.021.

Kaus, B., and Y. Podladchikov (2006), Initiation of localized shear zones in viscoelastoplastic rocks, *Journal of geophysical research*, *111*(B4), doi: 10.1029/2005JB003652.

Kidder, S., G. Hirth, J.-P. Avouac, and W. Behr (2016), The influence of stress history on the grain size and microstructure of experimentally deformed quartzite, *Journal of Structural Geology*, *83*, 194–206, doi: 10.1016/j.jsg.2015.12.004.

Kronenberg, A. K., S. H. Kirby, and J. Pinkston (1990), Basal slip and mechanical anisotropy of biotite, *Journal of geophysical research*, *95*(B12), 19,257–19,278, doi: 10.1029/jb095ib12p19257.

Lawlis, J. D. (1998), *High temperature creep of synthetic olivine-enstatite aggregates*, The Pennsylvania State University.

Liao, J., Q. Wang, T. Gerya, and M. D. Ballmer (2017), Modeling craton destruction by hydration-induced weakening of the upper mantle, *Journal of Geophysical Research, [Solid Earth]*, *122*(9), 7449–7466, doi: 10.1002/2017jb014157.

Linckens, J., M. Herwegh, O. Muntener, and I. Mercolli (2011), Evolution of a polymineralic mantle shear zone and the role of second phases in the localization of deformation, *Journal of Geophysical Research, [Solid Earth]*, *116*.

Linckens, J., M. Herwegh, and O. Müntener (2015), Small quantity but large effect — how minor phases control strain localization in upper mantle shear zones, *Tectonophysics*, *643*, 26–43, doi: 10.1016/j.tecto.2014.12.008.

Marti, S., H. Stünitz, R. Heilbronner, O. Plümper, and M. Drury (2017), Experimental investigation of the brittle-viscous transition in mafic rocks – interplay between fracturing, reaction, and viscous deformation, *Journal of Structural Geology*, *105*, 62–79, doi: 10.1016/j.jsg.2017.10.011.

Marti, S., H. Stünitz, R. Heilbronner, O. Plümper, and R. Kilian (2018), Syn-kinematic hydration reactions, grain size reduction, and dissolution–precipitation creep in experimentally deformed plagioclase–pyroxene mixtures, *Solid earth*, *9*(4), 985–1009, doi: 10.5194/se-9-985-2018.

Matysiak, A. K., and C. A. Trepmann (2015), The deformation record of olivine in mylonitic peridotites from the finero complex, ivrea zone: Separate deformation cycles during exhumation, *Tectonics*, *34*(12), 2514–2533, doi: 10.1002/2015tc003904.

Menegon, L., H. Stünitz, P. Nasipuri, R. Heilbronner, and H. Svahnberg (2013), Transition from fracturing to viscous flow in granulite facies perthitic feldspar (lofoten, norway), *Journal of Structural Geology*, *48*, 95–112, doi: 10.1016/j.jsg.2012.12.004.

Montési, L. G. J. (2007), A constitutive model for layer development in shear zones near the brittle-ductile transition, *Geophysical research letters*, *34*(8), doi: 10.1029/2007gl029250.

Montési, L. G. J. (2013), Fabric development as the key for forming ductile shear zones and enabling plate tectonics, *Journal of Structural Geology*, *50*, 254–266, doi: 10.1016/j.jsg.2012.12.011.

Moresi, L., F. Dufour, and H.-B. Mühlhaus (2003), A lagrangian integration point finite element method for large deformation modeling of viscoelastic geomaterials, *Journal of computational physics*, *184*(2), 476–497, doi: 10.1016/s0021-9991(02)00031-1.

Ohuchi, T., S.-I. Karato, and K. Fujino (2011), Strength of single-crystal orthopyroxene under lithospheric conditions, *Contributions to mineralogy and petrology. Beitrage zur Mineralogie und Petrologie*, *161*(6), 961–975, doi: 10.1007/s00410-010-0574-3.

Oliot, E., P. Goncalves, and D. Marquer (2010), Role of plagioclase and reaction softening in a metagranite shear zone at mid-crustal conditions (gotthard massif, swiss central alps), *Journal of Metamorphic Geology*, *28*(8), 849–871, doi: 10.1111/j.1525-1314.2010.00897.x.

Platt, J. P., and W. M. Behr (2011), Grainsize evolution in ductile shear zones: Implications for strain localization and the strength of the lithosphere, *Journal of Structural Geology*, *33*(4), 537–550, doi: 10.1016/j.jsg.2011.01.018.

Rast, M., and J. B. Ruh (2021), Numerical shear experiments of quartz-biotite aggregates: Insights on strain weakening and two-phase flow laws, *Journal of Structural Geology*, *149*(104375), 104,375, doi: 10.1016/j.jsg.2021.104375.

Rast, M., A. Galli, J. B. Ruh, M. Guillong, and C. Madonna (2022), Geology along the bedretto tunnel: kinematic and geochronological constraints on the evolution of the gotthard massif (central alps), *Swiss Journal of Geosciences*, *115*(1).

Richter, B., H. Stünitz, and R. Heilbronner (2018), The brittle-to-viscous transition in polycrystalline quartz: An experimental study, *Journal of Structural Geology*, *114*, 1–21, doi: 10.1016/j.jsg.2018.06.005.

Rozel, A., Y. Ricard, and D. Bercovici (2011), A thermodynamically self-consistent damage equation for grain size evolution during dynamic recrystallization, *Geophysical Journal International*, *184*(2), 719–728, doi: 10.1111/j.1365-246X.2010.04875.x.

Ruh, J. B., and J. Vergés (2018), Effects of reactivated extensional basement faults on structural evolution of fold-and-thrust belts: Insights from numerical modelling applied to the kopet dagh mountains, *Tectonophysics*.

Ruh, J. B., L. Tokle, and W. M. Behr (2022), Grain-size-evolution controls on lithospheric weakening during continental rifting, *Nature geoscience*, *15*(7), 585–590, doi: 10.1038/s41561-022-00964-9.

Rutter, E. H., and K. H. Brodie (1988), The role of tectonic grain size reduction in the rheological stratification of the lithosphere, *Geologische Rundschau: Zeitschrift fur allgemeine Geologie*, *77*(1), 295–307, doi: 10.1007/bf01848691.

Rutter, E. H., and K. H. Brodie (2004), Experimental grain size-sensitive flow of hot-pressed brazilian quartz aggregates, *Journal of Structural Geology*, *26*(11), 2011–2023, doi: 10.1016/j.jsg.2004.04.006.

Rybacki, E., and G. Dresen (2000), Dislocation and diffusion creep of synthetic anorthite aggregates, *Journal of geophysical research*, *105*(B11), 26,017–26,036, doi: 10.1029/2000JB900223.

Rybacki, E., and G. Dresen (2004), Deformation mechanism maps for feldspar rocks, *Tectonophysics*, *382*(3-4), 173–187, doi: 10.1016/j.tecto.2004.01.006.

Rybacki, E., M. Gottschalk, R. Wirth, and G. Dresen (2006), Influence of water fugacity and activation volume on the flow properties of fine-grained anorthite aggregates, *Journal of Geophysical Research, [Solid Earth]*, *111*(B3).

Schierjott, J., A. Rozel, and P. Tackley (2020a), On the self-regulating effect of grain size evolution in mantle convection models: application to thermochemical piles, *Solid earth*, *11*(3), 959–982, doi: 10.5194/se-11-959-2020.

Schierjott, J. C., M. Thielmann, A. B. Rozel, G. J. Golabek, and T. V. Gerya (2020b), Can grain size reduction initiate transform faults?—insights from a 3-d numerical study, *Tectonics*, *39*(10), e2019TC005,793, doi: 10.1029/2019tc005793.

Schön, J. H. (2015), *Physical properties of rocks*, Handbook of Petroleum Exploration and Production, 2 ed., Elsevier, Amsterdam.

Shea, W. T., and A. K. Kronenberg (1992), Rheology and deformation mechanisms of an isotropic mica schist, *Journal of Geophysical Research, [Solid Earth]*, *97*(B11), 15,201–15,237.

Shinevar, W. J., M. D. Behn, and G. Hirth (2015), Compositional dependence of lower crustal viscosity, *Geophysical research letters*, *42*(20), 8333–8340.

Skemer, P., and S.-I. Karato (2007), Effects of solute segregation on the grain-growth kinetics of orthopyroxene with implications for the deformation of the upper mantle, *Physics of the Earth and Planetary Interiors*, *164*(3-4), 186–196, doi: 10.1016/j.pepi.2007.06.011.

Speciale, P. A., W. M. Behr, G. Hirth, and L. Tokle (2020), Rates of olivine grain growth during dynamic recrystallization and postdeformation annealing, *Journal of Geophysical Research, [Solid Earth]*, *125*(11), doi: 10.1029/2020jb020415.

Speciale, P. A., L. Tokle, and W. M. Behr (2022), Feldspar and orthopyroxene piezometers constrained using quartz–feldspar and olivine–orthopyroxene mineral pairs from natural mylonites, *Journal of Structural Geology*, *154*(104495), 104,495, doi: 10.1016/j.jsg.2021.104495.

Stipp, M., and J. Tullis (2003), The recrystallized grain size piezometer for quartz, *Geophysical research letters*, *30*(21), doi: 10.1029/2003gl018444.

Stipp, M., H. Stunitz, R. Heilbronner, and S. M. Schmid (2002), The eastern tonale fault zone: a 'natural laboratory' for crystal plastic deformation of quartz over a temperature range from 250 to 700 degrees C, *Journal of Structural Geology*, *24*(12), 1861–1884.

Thielmann, M., and B. J. P. Kaus (2012), Shear heating induced lithospheric-scale localization: Does it result in subduction?, *Earth and planetary science letters*, *359-360*, 1–13, doi: 10.1016/j.epsl.2012.10.002.

Tokle, L., and G. Hirth (2021), Assessment of quartz grain growth and the application of the wattmeter to predict quartz recrystallized grain sizes, *Journal of Geophysical Research, [Solid Earth]*, *126*(7), doi: 10.1029/2020jb021475.

Tokle, L., G. Hirth, and W. M. Behr (2019), Flow laws and fabric transitions in wet quartzite, *Earth and planetary science letters*, *505*, 152–161, doi: 10.1016/j.epsl.2018.10.017.

Tokle, L., G. Hirth, and H. Stünitz (2023), The effect of muscovite on the microstructural evolution and rheology of quartzite in general shear, *Journal of Structural Geology*, *169*(104835), 104,835, doi: 10.1016/j.jsg.2023.104835.

Tommasi, A., A. Vauchez, L. A. D. Femandes, and C. Porcher (1994), Magma-assisted strain localization in an orogen-parallel transcurrent shear zone of southern brazil, *Tectonics*, *13*(2), 421–437, doi: 10.1029/93TC03319.

Trouw, R. A. J., C. W. Passchier, and D. J. Wiersma (2009), *Atlas of Mylonites - and related microstructures*, Springer Science & Business Media.

Tullis, J., R. Yund, and J. Farver (1996), Deformation-enhanced fluid distribution in feldspar aggregates and implications for ductile shear zones, *Geology*, *24*(1), 63, doi: 10.1130/0091-7613(1996)024<0063:defdif>2.3.co;2.

Van der Wal, D., P. Chopra, M. Drury, and J. D. Fitz Gerald (1993), Relationships between dynamically recrystallized Grain-Size and deformation conditions in experimentally deformed olivine rocks, *Geophysical research letters*, *20*(14), 1479–1482.

Vauchez, A., A. Tommasi, and D. Mainprice (2012), Faults (shear zones) in the earth's mantle, *Tectonophysics*, *558-559*, 1–27, doi: 10.1016/j.tecto.2012.06.006.

Viegas, G., L. Menegon, and C. Archanjo (2016), Brittle grain-size reduction of feldspar, phase mixing and strain localization in granitoids at mid-crustal conditions (pernambuco shear zone, NE brazil), *Solid earth*, *7*(2), 375–396, doi: 10.5194/se-7-375-2016.

Vissers, R. L. M., M. R. Drury, E. H. Hoogerduijn, C. J. Spiers, and D. J. T. Van der Wal (1995), Mantle shear zones and their effect on lithosphere strength during continental breakup, *Tectonophysics*, *249*(3-4), 155–171.

Walker, A. N., E. H. Rutter, and K. H. Brodie (1990), Experimental study of grain-size sensitive flow of synthetic, hot pressed calcite rocks, in *Deformation Mechanisms, Rheology, and Tectonics*, vol. Special Publication 54, edited by R. J. Knipe and E. H. Rutter, pp. 259–284, Geological Society of London.

Warren, J. M., and G. Hirth (2006), Grain size sensitive deformation mechanisms in naturally deformed peridotites, *Earth and planetary science letters*, *248*(1-2), 438–450, doi: 10.1016/j.epsl.2006.06.006.

Zhang, G., S. Mei, M. Song, and others (2017), Diffusion creep of enstatite at high pressures under hydrous conditions, *Journal of geophysical research*, *122*(10), 7718–7728.

Zhang, G., S. Mei, and M. Song (2020), Effect of water on the dislocation creep of enstatite aggregates at 300 MPa, *Geophysical research letters*, *47*(5), doi: 10.1029/2019gl085895.